ARMY RESEARCH LABORATORY

Brain Structure-function Couplings (FY11)

by Jean Vettel, Amy Dagro, Stephen Gordon, Scott Kerick, Reuben Kraft, Samantha Luo, Sandhya Rawal, Manny Vindiola, and Kaleb McDowell

ARL-TR-5893 **January 2012**

NOTICES

Disclaimers

The findings in this report are not to be construed as an official Department of the Army position unless so designated by other authorized documents.

Citation of manufacturer's or trade names does not constitute an official endorsement or approval of the use thereof.

Destroy this report when it is no longer needed. Do not return it to the originator.

Army Research Laboratory
Aberdeen Proving Ground, MD 21005

ARL-TR-5893 **January 2012**

Brain Structure-function Couplings (FY11)

Jean Vettel, Scott Kerick, Samantha Luo, Sandhya Rawal, and Kaleb McDowell
Human Research and Engineering Directorate, ARL

Amy Dagro and Reuben Kraft
Weapons and Materials Research Directorate, ARL

Stephen Gordon
DCS Corporation
Alexandria, VA

Manny Vindiola
Dynamics Research Corporation
Andover, MA

REPORT DOCUMENTATION PAGE

Form Approved
OMB No. 0704-0188

1. REPORT DATE *(DD-MM-YYYY)*	2. REPORT TYPE	3. DATES COVERED (From - To)
January 2012	DSI	1 October 2010 to 30 September 2011

4. TITLE AND SUBTITLE
Brain Structure-function Couplings (FY11)

5a. CONTRACT NUMBER

5b. GRANT NUMBER

5c. PROGRAM ELEMENT NUMBER

6. AUTHOR(S)
Jean Vettel, Amy Dagro, Stephen Gordon, Scott Kerick, Reuben Kraft, Samantha Luo, Sandhya Rawal, Manny Vindiola, and Kaleb McDowell

5d. PROJECT NUMBER

5e. TASK NUMBER

5f. WORK UNIT NUMBER

7. PERFORMING ORGANIZATION NAME(S) AND ADDRESS(ES)
U.S. Army Research Laboratory
ATTN: RDRL-HRS-C
Aberdeen Proving Ground, MD 21005

8. PERFORMING ORGANIZATION REPORT NUMBER
ARL-TR-5893

9. SPONSORING/MONITORING AGENCY NAME(S) AND ADDRESS(ES)

10. SPONSOR/MONITOR'S ACRONYM(S)

11. SPONSOR/MONITOR'S REPORT NUMBER(S)

12. DISTRIBUTION/AVAILABILITY STATEMENT
Approved for public release; distribution unlimited.

13. SUPPLEMENTARY NOTES

14. ABSTRACT

In FY11, a collaborative team of researchers began a new Director's Strategic Initiative (DSI) to examine brain structure-function couplings. The effort aims to develop a multidisciplinary, multiscale understanding of the relationship between the brain's physical structure, its dynamic electrochemical functioning, and human behavior. Here, brain structure refers to the architecture of the brain, namely, the grey matter regions in the brain and the white matter fiber tracts that connect them, and brain function indicates the neuron activity that enables communication between those regions. Combined, the individual variations in brain structure and function are thought to underlie and predict individual differences in task performance and human behavior. One of the broad, far-reaching goals of this initiative is to understand the set of circumstances under which individual differences in brain structure can be leveraged to account, predict, or enhance the measurement of brain function at varying time scales. The initiative has four main research areas—electrochemical modeling, biomechanical structural changes, electrochemical data collection and analysis, and time-evolving functional connectivity—and this year-end report captures some of the research highlights and accomplishments during the first year of the program.

15. SUBJECT TERMS
Brain structure, white matter fiber tracts, brain function, EEG, functional connectivity, phase synchronization, finite element model, Director's Strategic Initiative (DSI)

16. SECURITY CLASSIFICATION OF:			17. LIMITATION OF ABSTRACT	18. NUMBER OF PAGES	19a. NAME OF RESPONSIBLE PERSON
a. REPORT	b. ABSTRACT	c. THIS PAGE			Jean Vettel
Unclassified	Unclassified	Unclassified	UU	80	19b. TELEPHONE NUMBER (*Include area code*) (410) 278-7431

Standard Form 298 (Rev. 8/98)
Prescribed by ANSI Std. Z39.18

Contents

List of Figures vi

List of Tables viii

Acknowledgments ix

1. Overview: Brain Structure-Function Couplings 1

1.1 Objective 1

1.2 Program Overview 1

1.2.1 Near-term Goals 3

1.2.2 Summary 7

1.3 Report Overview 8

1.4 Year 1 Transitions (Oct 2010–Sept 2011) 9

2. Project 1: WPLI as a Method for Identifying Task-Related Functional Networks in EEG Recordings during a Shooting Task 12

2.1 Authors 12

2.2 Introduction 12

2.3 Methods or Approach 13

2.3.1 Participants 13

2.3.2 EEG Acquisition 13

2.3.3 Task and Event Extraction 14

2.3.4 EEG Pre-processing 14

2.3.5 Analysis 14

2.4 Results and Discussion 15

2.5 Conclusions 18

3. Project 2: Functional Connectivity of EEG Data Using the Weighted Phase Lag Index (WPLI): Robustness to Artifacts in Real-world Environments 18

3.1 Authors 18

3.2 Introduction 18

3.2.1 Objective 20

3.3 Methods or Approach 21

3.3.1 Participants 21
3.3.2 Task and Event Extraction 21
3.3.3 EEG Acquisition 22
3.3.4 EEG Pre-processing 22
3.3.5 Weighted Phase Lag Index (WPLI) 24
3.4 Results and Discussion 25
3.4.1 Spectral Power 25
3.4.2 Weighted Phase Lag Index 26
3.5 Conclusions 29

4. Project 3: Validating Functional Connectivity Measures Using Neural Mass Models 29
4.1 Authors 29
4.2 Introduction 30
4.2.1 Objective 31
4.3 Methods or Approach 31
4.3.1 Neural Mass Models 31
4.3.2 Simulation Structure 35
4.3.3 Functional Connectivity Measures 35
4.4 Results and Discussion 36
4.4.1 Result 1: Validation of the Neural Mass Models 36
4.4.2 Result 2: Limitation of ImC and dWPLI 40
4.4.4 Result 3: dWPLI Has Greatest Sensitivity in Low Frequency Bands 41
4.5 Conclusions 42

5. Project 4: Design and Implementation of a Numerical Technique to Inform Anisotropic Hyperelastic Finite Element Models Using Diffusion-weighted Imaging 44
5.1 Authors 44
5.2 Introduction 44
5.3 Methods, Results, and Discussion 46
5.3.1 Continuum Theory of Transversely Isotropic Hyperelasticity 46
5.3.2 Validation of Numerical Method 50
5.3.3 An Algorithm for Linking DTI and Continuum Mechanics 51
5.3.4 A Scheme for Averaging Multiple Fibers 55
5.3.5 Application to Modeling White Matter Tissue of the Human Brain 58
5.4 Conclusions 59

6. Conclusion 60

7. References **61**

Lists of Symbols, Abbreviations, and Acronyms **66**

Distribution List **68**

List of Figures

Figure 1. The initiative investigates how couplings between individual variation in brain structure and brain function can be linked to individual differences in human behavior. 1

Figure 2. The nervous system can be described at multiple spatial scales for both brain structure (left) and brain function (right). 3

Figure 3. An overview of the four main research areas in the DSI on Brain Structure-Function Couplings, a brief description of their scientific products, and how the areas are envisioned to intersect with one another. 8

Figure 4. (a) The map of electrodes depicted highlights the electrodes with significance in black. (b) The map of electrodes depicted highlights the nonzero phase lag statistical interdependencies identified by WPLI with black lines between the interdependent electrodes. The location of each electrode is the same as in a. 15

Figure 5. (a) The WPLI analysis depicted was conducted in the theta band, 4–8 Hz, on the Fz and CP3 electrode. Thirty significant points were found from –290 to 0 ms before the trigger pull, (b) the WPLI analysis depicted was conducted in the theta band, 4–8 Hz, on the FC3 and Pz electrode. Thirty significant points were found from –2990 to –2700 ms before the trigger pull, (c) the WPLI analysis depicted was conducted in the delta band, 1–4 Hz, on the F8 and P02 electrode. Thirty-two significant points were found from –2910 to–2600 ms before the trigger pull, and (d) the WPLI analysis depicted was conducted in the theta band, 4–8 Hz, on the C3 and Pz electrode. Sixty-four significant points were found from –2990 to –2360 ms before the trigger pull. 17

Figure 6. Example illustrating three types of events extracted from continuous EEG channel data. (Top to bottom): (1) non-event-related artifact, (2) transient alpha bursting, and (3) event-related artifact. Note that these signals are from data prior to epoching and that a longer than 3 s time window is illustrated. 22

Figure 7. Channel power by event and frequency band for each of the 50 individual trials. Within each plots, trials are sorted by the length of the EEG event (shorter events on top). Three of the six frequency bands (theta, alpha II, gamma) are plotted in columns. All three event types (Random, Alpha, and Trigger) are plotted in rows. A black bar below each plot shows when the distributions of power values were significantly higher than baseline (–1 0 s). 24

Figure 8. WPLI by event and frequency band for each of the 50 individual trials. Within each plot, trials are sorted by the length of the EEG event (shorter events on top). Three of the six frequency bands (theta, alpha II, gamma) are plotted in columns. All three event types (Random, Alpha, and Trigger) are plotted in rows. A black bar below each plot shows when the distributions of power values were significantly higher than baseline [–1 0 s]. A red bar below each plot shows when the distributions of WPLI were significantly higher than baseline [–1 0 s]. 27

Figure 9. The time course of a single region in a NMM in isolation with two internal subpopulations. The output is generated by nonlinearly combining a weighted mixture of 80% from a subpopulation oscillating at 11 Hz and 20% from a subpopulation oscillating at 43 Hz. 32

Figure 10. Architecture of two interconnected neural mass regions. Each region is composed from three columnar layers. The excitatory spiny stellate layer receives the external input coming from other regions. The pyramidal layer sends output to other regions. The interaction between the excitatory spiny stellate and inhibitory interneuron layers give rise to oscillatory activation patterns in the pyramidal layer. Each region may have multiple subpopulations, each of which drives oscillations at a different fundamental frequency. In this figure, region 1 has three internal subpopulations and region 2 has two. ✚ is the weighted sum of the sub-populations and S is the sigmoid function. 33

Figure 11. The seven possible combinations of 10- and 40-Hz peaked oscillator pairs over two connection types.....35

Figure 12. Time course and PSD plots for two pairs of identical bicoupled neural mass regions. Time courses show that they produce oscillatory firing patterns, and the firing rate increases greatly when the coupling is on (1–3 s and 5–8 s). Power spectral density plots show that both units have the same power distribution both when the coupling is off and on. When coupling is on, both regions show a small downshift in the peak frequency as well as a large increase in power at that frequency and its second harmonic. 37

Figure 13. Time course and power spectral density plots for two pairs of NMMs. Time courses show that they produce oscillatory firing patterns and the firing rate increases greatly when the coupling is on (1–3 s and 5–8 s). Power spectral density plots show that the power distribution is different when coupling is off compared to when it is on. 38

Figure 14. Power-frequency plots for 10 Hz ←→ 40 Hz pair when coupling is off and on. When the coupling is off, both units have a unimodal power distribution centered at their respective dominant frequencies. When coupling is on both units have a bimodal power distribution. One peak comes from the unit's intrinsic oscillation rate and the other arises because influences from the other unit. The most interesting part is that the coupling causes a frequency downshift in both units. The 10-Hz unit has peaks at 8 and 35 Hz and the 40-Hz unit has power peaks at 3, 7, 35, and 66 Hz.....39

Figure 15. Phase-based functional connectivity estimates using PLV, ImC and dWPLI. Only PLV is able to identify 30–50 Hz phase synchronization but the measure also has a strong tendency to incorrectly identify phase synchronizations at lower frequencies regardless of whether the coupling is on or off. ImC and dWPLI fail to identify phase synchronizations at any frequency. 40

Figure 16. (D) Phase-based functional connectivity estimates using PLV, ImC and dWPLI. All three measures identify 20–60 Hz phase synchronizations when coupling is on but in the lower 1–5 Hz frequency range, only dWPLI identifies a reliable difference in phase synchronization. 42

Figure 17. Using DTI, axonal fiber tractography can be overlaid on a finite element mesh and used to construct a transversely isotropic model. Tractography consists of complex fibers shown from (b) dorsal, (c) right lateral side, and (d) posterior views. 45

Figure 18. Comparison between the finite element results and analytic solutions for three different loading conditions: (a) uniaxial, (b) strip biaxial, and (c) equibiaxial. 51

Figure 19. Fiber discretization and notation definitions used throughout the report. 52

Figure 20. Schematic of the various cases that are possible when determining if a fiber segment (within a given tractography fiber) overlaps with a finite element in space. 53

Figure 21. Method used to test if a specified point is within the element. Algorithms for both tetrahedron and hexahedron elements are designed and implemented. 53
Figure 22. Method used to test if a line intersects the faces of an element for the case in which the line segment intersects the element faces, but no points in the segment reside within the element (see Case 4 in figure 20). 54
Figure 23. Depending on the fiber or mesh densities, there could be multiple fibers, or multiple fiber segments, or both existing in a single element which requires an averaging scheme. 56
Figure 24. The sum of the vectors will give an average orientation. 56
Figure 25. The global algorithm used to obtain final vector orientations for each element. 57
Figure 26. Averaging fibers that are not fully contained in the element can create a misrepresented average direction for the individual element. 58
Figure 27. DTI input data versus the assigned orientation output. 59

List of Tables

Table 1. Latency ranges (low–high ms) of significant power increase for each event type and frequency band. 25
Table 2. Latency ranges (low–high ms) of significant WPLI increase for each event type and frequency band. 28

Acknowledgments

We would like to acknowledge Peter Chung (Computational and Information Sciences Directorate [CISD]) and his intellectual contributions that were a critical component during the development of this collaborative project. We would also like to thank Brian Henz, Robert Fernandez, Piotr Franaszczuk, and Troy Lau for helpful discussions about the research and/or this report.

INTENTIONALLY LEFT BLANK.

1. Overview: Brain Structure-Function Couplings

1.1 Objective

This overview aims to capture the general direction of this evolving program as developed by the collaborators on the initiative.

1.2 Program Overview

Every individual has a unique set of talents and skills, and these individual differences manifest in the speed and accuracy of behavioral responses across tasks, the strategies employed to solve problems, and the reactions to challenging experiences, to name just a few. Individuals have unique capabilities, and researchers have attempted to explain these differences in human behavior for centuries. Many disciplines have relied on behavior alone, but the field of neuroscience capitalizes on continual advancements in brain imaging methodologies, computational approaches, and modeling techniques to better understand and predict the interaction between the brain and behavior. By studying neural processing mechanisms in the brain, neuroscientists hope to unravel how the brain enables the mind.

Recent advancements in neuroimaging technologies and computational analysis capabilities have enabled new approaches for understanding the basic principles of brain organization and function. The research initiative on brain structure-function couplings capitalizes on some of these advancements to examine how differences in brain structure and brain function can be linked to differences in human behavior (figure 1).

Figure 1. The initiative investigates how couplings between individual variation in brain structure and brain function can be linked to individual differences in human behavior.

The brain consists of both grey matter, primarily neuronal cell bodies and glial cells, and white matter, myelinated axons that transmit electrochemical signals between grey matter regions. The grey matter is heterogeneous. Different regions of the brain, often referred to as Brodmann's areas after the scientist who pioneered and popularized a particular parcellation scheme, have different cellular properties and structure, and the field of cytoarchitectonics examines how grey

matter is structured. A complementary field of myeloarchitectonics examines how axons are structured. Although grey matter regions, such as the aforementioned Brodmann areas, are largely preserved between people, these regions will differ in size, shape, location, and cytoarchitecture across individuals. Likewise, major fiber tract bundles of axons that connect particular grey matter regions are preserved across people, but the tracts within the bundle vary in the total number, projection path, termination location, and myeloarchitecture of the tracts between individuals. These numerous sources of individual structural variation hold potential for explaining individual differences in neuronal activity within a grey matter region and neural communication between regions. Critically, recent advancements in structural neuroimaging technologies, known as diffusion weighted imaging techniques, provide a new capability to image white matter fiber tracts noninvasively in human volunteers. These new white matter imaging techniques can be combined with existing robust, structural imaging measures for grey matter. Within the past decade, the neuroscience field, including this research initiative, is just beginning to examine approaches that best utilize these structural imaging techniques in conjunction with functional imaging data of brain activity and measurements of human behavior.

Similar to structural variation, there are also numerous sources of functional variation between people. The electrochemical activity within a region has spatial topologies and temporal dependencies dependent on the cytoarchitecture of the grey matter itself. These variations reflect concentrations of neurotransmitters, organization of synapses, refractory periods for these various electrochemical processes, etc. Likewise, the transmission time and projection path of a neuronal signal depends on the myeloarchitecture of the fiber tracts, as well as lower level electrochemical properties of the tracts themselves. These structural constraints of functional activity are expected across these spatial scales within a physical system, but the current imaging technologies cannot easily measure the available resources and dynamic structure at each of these levels. Consequently, our research efforts emphasize functional parameters and structure that can be imaged noninvasively in human subjects, and in particular, this research initiative also exploits recent developments in functional connectivity analysis techniques. Traditionally, functional analysis methods have focused on individual differences in localization of brain activity. For example, studies may identify whether a particular grey matter region is activated across people, or whether the timing of a neural response within a region is the same between different tasks. Functional connectivity approaches emphasize the global dynamics and topology of brain activity. While some functional connectivity research has looked at coupled activity between pairs of brain regions, recent innovative approaches have started examining the properties of larger networks and computing connectivity across multiple regions simultaneously. These newly developed methods emphasize a systems-level or network-level description of communication across the brain, providing an opportunity to leverage insights from network science.

Combined, the new imaging methods for structural connections and the novel methodologies for understanding global functional connectivity provide a promising avenue to examine the link

between structural variation and functional variation across individuals. These developments hold promise to identify individual variations that can be linked to differences in human behavior. Importantly, this initiative emphasizes the development of imaging measurements and analysis methods that capture statistically meaningful differences between individuals. If the predictive capability between structure, function, and behavior is realized, brain metrics can be used in a host of applications ranging from neurotechnologies that optimize Soldier-system performance, to training technologies that decrease time to train, to assessments of whether injured Soldiers should return to battle. In short, this initiative addresses a fundamental question in neuroscience about the predictive coupling between variations in brain structure and brain function, and if it is successful, it will have broad-based application to the Army.

1.2.1 Near-term Goals

For the near-term goals of this initiative in Brain Structure-Function Couplings, we feel it is important to focus on particular scales of nervous system organization. Like other multiscale modeling domains, the nervous system has important features at multiple spatial scales as well as multiple temporal scales within a given spatial scale. As visualized in figure 2, the spatial scales of brain structure range from genes and small proteins up through single neurons to local circuits within small areas of the cortex, all the way up to distributed networks of brain regions that enable global, whole-brain interactions.

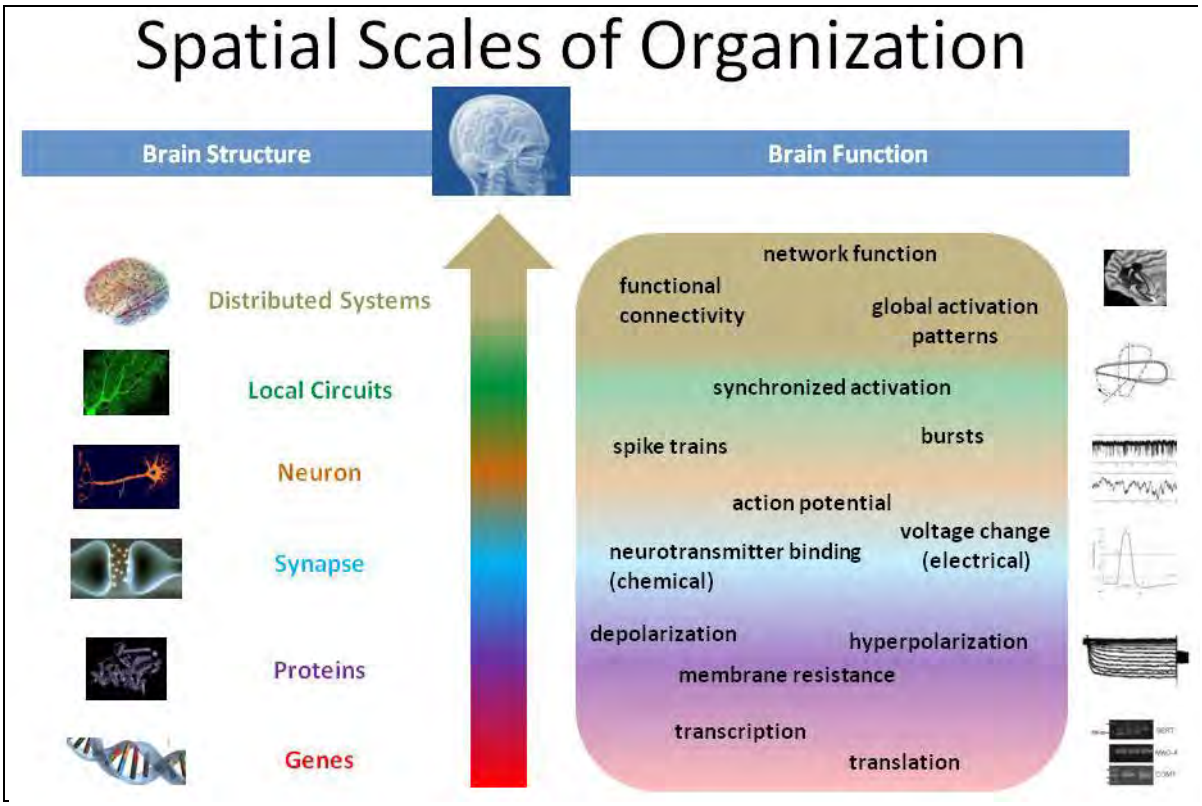

Figure 2. The nervous system can be described at multiple spatial scales for both brain structure (left) and brain function (right).

Likewise, brain function can also be measured and described at these multiple spatial scales. Recent modeling efforts like the Blue Brain project are using supercomputers to replicate the structure and function of local circuits known as cortical columns from thousands of experiments in the rat cortex (EFPL, 2011). The majority of the data is collected from single neurons within a cortical column that averages a total of 10,000 neurons, and computational algorithms are then built for the column and tested to see how well the model replicates the empirical data. Using this approach, the modeling effort intends to gradually build a replication of the entire rat cortex. Our Director's Strategic Initiative (DSI) effort is *not* aimed at building a replication of whole-brain activity in humans; instead, our research efforts focus on the circuit and distributed system scales, examining if network-level brain *structural* organization and/or network-level brain *functional* activation patterns are predictive of task-relevant brain states. These scales were largely selected based on current neuroimaging modalities that measure global brain activity and ongoing innovations for imaging structural networks and computing functional connectivity. To this end, we examine the circuit and distributed system scale of nervous system organization in two complementary efforts: an empirical effort and a modeling effort. Critically, these two research efforts, and the two studied spatial scales, must intersect. Our group has chosen to leverage the Connectome approach (Bullmore and Sporns, 2009) where graph theory serves as the framework for both structural and functional network descriptions.

Using a graph theoretic framework, a common scheme is used to generate a structural brain graph and a functional brain graph to capture an individual's network properties. Brain regions are considered nodes on the graph, and connections between those regions are the edges. For either type of graph, the nodes of the graph must first be determined by dividing the grey matter of the brain into smaller regions, a process that relies on imaging an individual's brain anatomy using a magnetic resonance imaging (MRI) scanner. Brain regions used as graph nodes could be very coarse and segment the cortex into the four major cortical lobes (occipital, temporal, parietal, and frontal), smaller grey matter regions could be defined using a standard atlas (e.g., Harvard-Oxford atlas), task-specific regions could be identified by a functional dataset, or regions could be defined by numerous other parcellation methods. Once graph nodes are defined, the edges can be separately defined for the structural graph and the functional graph. The edges for an individual's structural graph are defined by the white matter fiber tract connections among the brain regions used as graph nodes. An individual's fiber tracts are collected using a diffusion-weighted imaging (DWI) scan on a MRI scanner, and the location and direction of the white matter tracts are inferred from the constrained movement of water molecules (see Hagmann et al., 2006 for a review). The edges for a functional graph are defined by a statistical coupling between the recorded brain activity across multiple brain regions. Consequently, functional graphs can be computed from time series of an individual's brain activity collected using any one of several different neuroimaging techniques such as electroencephalography (EEG), functional magnetic resonance imaging (fMRI), magnetoencephalography (MEG), etc. The end result is a graph with connections between nodes, providing a common framework for both structure and function within individuals. These graphs serve as the basis and the intersection for all of our

empirical and modeling efforts, as discussed in more detail below. In addition, these graphs provide a mechanism to incorporate temporal scales within our spatial scale of nervous system organization, as connection strengths between nodes can be altered to reflect learning/experience, brain damage, etc. Thus, the adopted graph theoretic framework lends itself to multiscale modeling efforts across both spatial and temporal scales.

As described in 1.2.1, our empirical research efforts aim to identify both structural and functional variations that are statistically meaningful indices of individual function and behavior. The first is a crude, but common, approach that directly examines the predictive relationship between differences in a structural parameter, such as fractional anisotropy (FA), and differences in task performance (Bengtsson et al., 2005; Cascio et al., 2007; Madden et al, 2004; Scholz et al., 2009). The work also examines relationships between functional analysis measures, both traditional and new connectivity measures, and differences in behavior. Thus, our work extends what structural and functional parameters are explored for predictive relationships with behavioral performance. Our second approach explores predictive links between structural parameters and differences in functional activation patterns, including the amplitude of the brain activity, latency of the activity, topography of the activation pattern, etc. Again, our research examines novel pairings of structural parameters and functional activity measures as well as their interactions with behavioral performance. Our third approach capitalizes on the adopted graph theory framework for the project. Numerous graph measures can be computed that capture features of a given network, such as its modularity, centrality, small worldliness, etc. (see Bassett et al., 2011 for a review of graph measures). Our group's working hypothesis is that this network-level description holds promise for identifying predictive couplings between individual variations in structure and function and their interactions with behavioral performance. Suppose the modularity of structural networks correlate with the ability of particular functional connectivity measures to capture a task-relevant brain activity pattern. Neurotechnologies can then be designed that match the most sensitive analysis method for the functional data based on the structural properties of a Soldier's brain. This third approach looks for predictive relationships within the properties of the structural and functional graphs themselves. Across all three approaches, the empirical efforts identify promising network parameters and/or connectivity patterns that capture meaningful individual variation and uses these parameters to help guide the modeling efforts.

This research initiative contains two modeling efforts: one is tied closely with the empirical efforts described previously and focuses on modeling electrochemical processing in the brain, while the second emphasizes the biomechanical response properties of brain tissue and hopes to bridge tissue damage to electrochemical processing disruptions/changes. Both efforts embody graph theory within their model. The electrochemical modeling effort simulates interconnected functional nodes that produce electrical activity at frequencies and temporal patterns controlled through parameterization of the model. This effort builds from David and Friston (2003) work to simulate the functional activity of small patches of cortex within each node. Many different

simulated networks can be implemented that have different numbers of nodes, different activity profiles within the nodes, different connectivity patterns among the nodes, communication between nodes at various timeframes, etc. Thus, this electrochemical modeling effort provides a mechanism to explore how different structural connections influence regional activity, functional connectivity, and global network properties. It also provides a testbed to examine measures of network properties. This modeling effort and the empirical research efforts are intended to refine and augment one another, as one is used to constrain or inform the other.

The other modeling effort, the biomechanical effort, focuses only on brain structure. Here, the graph nodes represent brain tissue with information about the white matter fiber tracts incorporated into the finite element model to better model brain tissue for simulation work. Research here is focused on developing a damage law that prescribes the brain tissue loading and response properties, based on empirical studies, for particular stress and strain rates at various orientations and durations. Simulations can then be run that predict damage to brain tissue, and this damage will then be transferred to a network framework so the model can produce a simulated structural graph that is altered to reflect the simulated tissue damage. For example, the connection strength between nodes may be decreased when the damage law hits a certain threshold or a node of the structural graph may be deleted at a different threshold value. By adopting the graph framework for representing simulated damage to the structural network, the biomechanical effort can link back to the electrochemical modeling and empirical research. The "damaged network" is another graph with different connections among nodes, and the electrochemical modeling effort provides a mechanism to explore how the functional activity changes due to these changes in the underlying network connections. This discussion of the modeling efforts highlights the importance of considering temporal scales within the study of structure-function couplings. Certainly in traumatic brain events, the network properties are changing as the injury dynamics unfold, but temporal scale is equally critical in healthy individuals and any attempt to link structural graphs and functional graphs has to acknowledge the substantial differences between their inherent timescales.

The near-term effort focuses on structure-function couplings based on a short-term snapshot of structural and functional graphs to establish the foundational principles; however, the long-term goal of the program is to develop time-evolving predictive models of structural variations that influence time-evolving models of global brain function and dynamic changes in cognitive performance. Both structural and functional connections change on varying timescales. Structural adaptations are inherently slow. Structural changes in professional concert pianists correlate with the number of adolescent practicing hours (Bengtsson et al., 2005), but structural changes have also been found after a few days of intensive training to juggle (Scholz et al., 2009). An individual's white matter pathways also reflect body mass index (Xu et al., 2011). However, structural changes can occur on very short timescales in conjunction with blast-induced or blunt force traumatic brain injuries (Taber et al., 2008). Likewise, functional adaptations can also reflect changes over different timescales. The brain constantly shifts

between stable brain states while performing a task. These changes can occur as quickly as 200 ms. Global patterns of functional activity have been correlated with predicted learning success on a new motor task across days (Bassett et al, 2011), but they also reflect long-term states, such as particular neural disorders (Stam et al, 2007). These examples highlight the range of meaningful timescales already identified in the literature, and the inherent challenge of linking the timescales of structural and functional changes where the timescales for measurable changes are quite different. Our near-term efforts are looking at short-term scales, establishing scaleable frameworks for future, time-evolving research efforts.

1.2.2 Summary

The Brain Structure-Function Couplings research effort addresses a basic Army challenge: how can we predict individual Soldier performance? This basic research (6.1) effort seeks to unravel the coupling between structural and functional variations that reflect individual differences from genetics, development, experience, training, etc., and link these differences to measurable differences in behavior.

The Army benefits, however, do not depend on the long-term achievement of the entire project. Each of the four research areas—electrochemical modeling, biomechanical structural changes, electrochemical data collection and analysis, and time-evolving functional connectivity—has been scoped to develop products to benefit the U.S. Army Research Laboratory (ARL) mission programs in the near-term (figure 3). The empirical work capitalizes on recent advancements in both structural imaging methods and global, functional connectivity measures in order to examine novel structural and functional parameters. These efforts are collecting new datasets with structural and functional data from the same individuals in collaboration with academic partners to explore couplings within Army relevant domains. Identifying novel metrics for individual differences will aid the development of individual-specific neurotechnologies. In concert, the electrochemical modeling effort examines basic principles of how structural connections effect functional relationships, allowing the empirical and modeling results to refine each other's future efforts. In particular, it currently serves as a critical test bed to evaluate if functional measures developed on empirical datasets capture the expected connectivity patterns in a simulation where the communication dynamics are known. Finally, the biomechanical modeling effort examines empirical-based approaches for developing damage laws the incorporate "injury physics" for brain tissue and ways to threshold and transfer this damage to a structural connectome. This effort increases the fidelity of simulations and can enhance Soldier protection technologies. Across all of the research efforts, this DSI in Brain Structure-Function couplings builds an in-house multidisciplinary expertise in computational brain modeling that is essential from basic needs for reviewing proposals to sophisticated efforts to identify modeling advancements that can be leveraged for Army problems

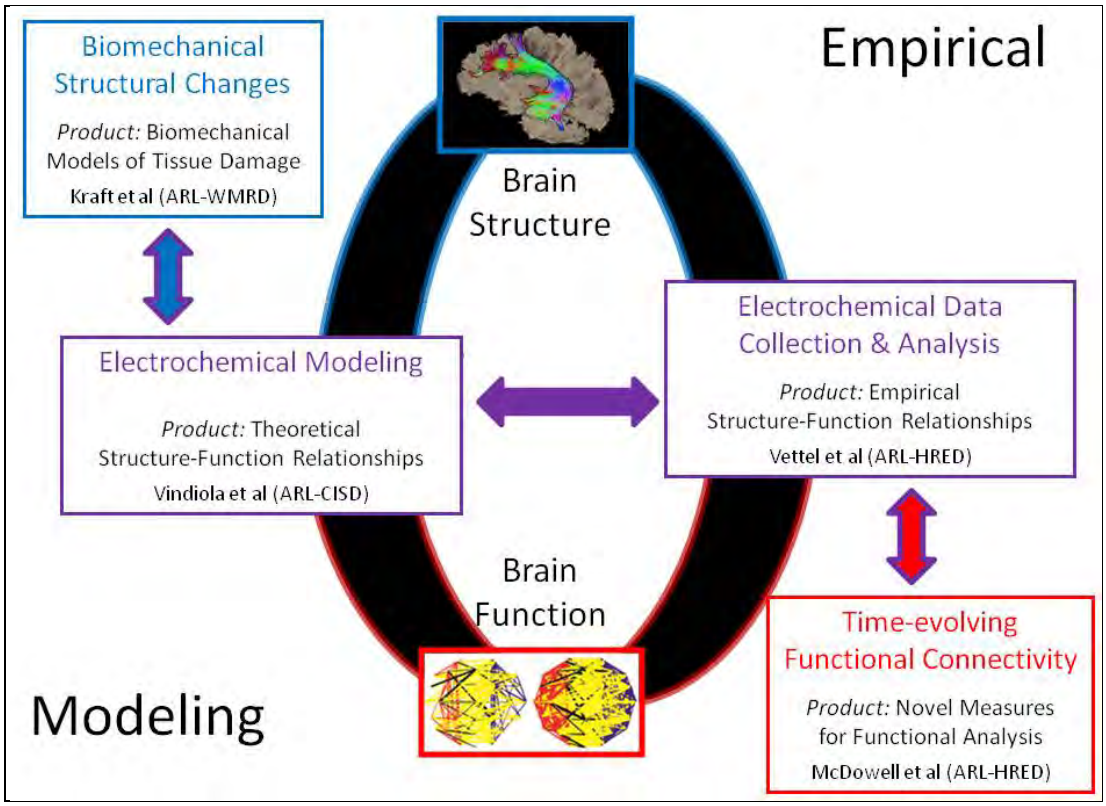

Figure 3. An overview of the four main research areas in the DSI on Brain Structure-Function Couplings, a brief description of their scientific products, and how the areas are envisioned to intersect with one another.

1.3 Report Overview

This report highlights a subset of Year 1 accomplishments in the program. Within the empirical efforts on electrochemical processes of the brain, we have chosen to highlight our work on functional measures this year. The first two projects describe complementary analyses of a previously collected EEG dataset where Soldiers used a demilitarized rifle in a target shooting task (Kerick et al., 2007). Both projects aim to evaluate if a functional connectivity measure, Weighted Phase Lag Index (WPLI) (Vinck et al., 2011), can successfully capture brain network dynamics in the presence of real-world movement artifacts. Project 1 is an exploratory analysis of one study participant, completed by a 2011 summer research intern, Sandhya Rawal. This first project compared the WPLI measure to a traditional time-frequency analysis, and the results indicated that the new connectivity measure captured at least three different brain activity patterns not identified by the traditional analysis approach. These preliminary results suggest that the method may have advantages over traditional approaches when the dataset has large-scale movement artifacts (ARL-TM-2011, 2011). In a complementary effort, Project 2 examines two properties of WPLI: its resilience to movement artifacts (in isolation and concurrent with task-relevant brain activity) and its sensitivity to brain activity (again, in isolation and concurrent with movement artifact). Across the 12 subjects analyzed, the measure was significant for brain-

related activity, but it was not significant for the artifacts (i.e., it was resilient against the noise artifacts). These results indicate that time-evolving WPLI holds promise for understanding brain function in complex operational environments with real-world eye and body movements, providing a critical tool for the development of neurotechnologies that could monitor neural data in real time to augment Soldier-system performance.

The final two projects described in this report showcase the accomplishments under the program's two modeling efforts—Project 3 describes progress under the electrochemical modeling research and Project 4 describes progress under the biomechanical modeling research (Kraft and Dagro, in press). In Project 3, a neural mass model that generates EEG-like simulated functional data was implemented. Several simulations of two-node networks verified the oscillatory behavior of the simulated brain regions (network nodes). The simulated EEG data was then analyzed using functional connectivity measures, including the time-evolving WPLI measure that was tested on the empirical datasets in Projects 1 and 2. Since the underlying functional activity is known, the simulation provides a powerful testbed for understanding and interpreting the results from the connectivity measures. The first round of simulation results indicate that the tested measures do capture the temporal dynamics of the communication between nodes, but even in two-node networks, the results indicate that network structure strongly influences the measure results and suggests relationships between structure and function need to be explored further. Finally, in Project 4, a method is described for incorporating anisotropic properties of biological tissue into a finite element model computational framework. The algorithm links the directionality information from empirically collected structural data, namely the white matter fiber tracts that connect brain regions, to the transverse isotropic model. This work lays the critical foundation needed to increase the fidelity of the brain tissue response in simulations of tissue damage due to blast or blunt forces.

Collectively, these four projects capture the research enhancements derived through cross-Directorate collaboration. The simulated EEG data can be used to validate and better understand functional measures that are tested on empirical datasets. The imaged brain structure is incorporated into a finite element model to increase the fidelity of the simulated tissue response properties. Critically, in our first year, each of the four efforts has successfully incorporated the Connectome-based, graph theoretic framework to ensure advancements between areas can be integrated as the research develops in the years to come.

1.4 Year 1 Transitions (Oct 2010–Sept 2011)

The following have been generated:

- Refereed Journal Papers:

    1. Lau, T. M.; Gwin, J. T.; McDowell, K.; Ferris, D. P. Weighted Phase Lag Index Stability as an Artifact Resistant Measure to Detect Cognitive EEG Activity During Locomotion. *Journal of NeuroEngineering and Rehabilitation*, submitted.

- Conference Presentations:

  1. Vettel, J; Bassett, D; Kraft, R; Grafton, S. Physics-based Models of Brain Structure Connectivity Informed by Diffusion-weighted Imaging. *Army Science Conference*, Nov 2010.

  2. Vettel, J; Bassett, D; Grafton, S. Reproducibility of Diffusion-weighted Imaging Across Multiple Scanning Sessions. *Society for Neuroscience*, Nov 2010.

- Government Reports:

  1. Kraft, R; Dagro, A. *Design and Implementation of a Numerical Technique to Inform Anisotropic Hyperelastic Finite Element Models using Diffusion Weighted Imaging*; (Project 4 in this report) ARL-TR-5796; U.S. Army Research Laboratory: Aberdeen Proving Ground, MD, in press.

  2. Rawal, S. *Weighted Phase Lag Index (WPLI) as a Method for Identifying Task-Related Functional Networks in Electroencephalography (EEG) Recordings during a Shooting Task*; (Project 1 in this report); ARL-TM-2011; U.S. Army Research Laboratory: Aberdeen Proving Ground, MD.

  3. Amrein, B. E.; Cassenti, D. N.; Cosenzo, K. A.; Krausman, A. S.; LaFiandra, M. E.; Lance, B. J.; Lockett, J. F.; McDowell, K. G.; Oie, K. S.; Rice-Berg, V. J.; Samms, C. L.; Vettel, J.M. (co-editors, alphabetical order). *Human Research and Engineering Directorate: Major Laboratory Programs: Current Thrust Areas and Recent Research*; ARL-SR-213; U.S. Army Research Laboratory: Aberdeen Proving Ground, MD, 2010.

- Collaborations/External Funding:

  1. Jean Vettel (Human Reearch and Engineering Directorate [HRED]) with Walt Schneider and Don Krieger at University of Pittsburgh (Collaborative Technology Alliances [CTA] seedling funds secured for data collection and joint analysis).

  2. Vettel (HRED) with Mike Miller, Barry Giesbrecht, and Scott Grafton at Institute for Collaborative Biotechnologies (ICB)/University of California at Santa Barbara (UCSB) (CTA seedlings funds secured for data collection and joint analysis as well as funds set aside for a joint postdoc to be hired in FY12).

  3. Vettel/Kaleb McDowell (HRED) funded Paul Sajda at Columbia University (task order funds secured for data collection and ARL analysis).

  4. Reuben Kraft (Weapons and Materials Research Directorate [WMRD]) sponsored United States Military Academy (USMA) Davies Fellow Project, “Influence of Brain Structure in NeuoTrauma Protection”.

  5. Kraft (WMRD) with Barclay Morrison at Columbia University.

6. Kraft (WMRD) with Rika Wright at Johns Hopkins University.
7. Kraft (WMRD) with University of Pennsylvania neural network Multidisciplinary University Research Initiative (MURI).
8. Kraft (WMRD) with Institute for Soldier Nanotechnologies.
9. Manuel Vindiola, Peter Chung, and Brian Henz (CISD) and Vettel (HRED) with Suvranu De and Alex Herzog at Rensselaer Polytechnic Institute.

- Personnel:
  1. Vindiola, a post-doc researcher from Johns Hopkins University hired as CISD postdoc to lead electrochemical modeling effort.
  2. Several student summer interns (Herzog – HRED/CISD, Rawal – HRED, Samantha Luo – HRED, Philip McKee – WMRD, etc.).
  3. Mentoring Science and Math Academy student on project "Modeling Damage in the *C. elegans* Structural Connectome" (WMRD, Kraft).
- Invited Cross-Service Briefs:
  1. McDowell, Medical Research and Materiel Command (MRMC), Feb 2011: "ARL's Neuroscience Strategic Research Initiative: Non-Injury."
  2. Chung, White House, Office of Science and Technology Policy (OSTP), March 2011: "Materials for Physical and Trauma Protection Deep Dive."
  3. McDowell and Vettel, Senate Arms Services Committee, Professional Staff Member, April 2011: "ARL Neuroscience" and "Brain Structure-Function Couplings."
  4. Kraft, ARO MURI, July 2011: "Computational Brain Biomechanics and Connections with the Human Connectome."
  5. McDowell and Vettel, Army Laboratory Assessment Group, July 2011: "ARL Neuroscience" and "Brain Structure-Function Couplings."
- Awards:
  1. Kraft: 2010 Presidential Early Career Award for Scientists and Engineers.
  2. Rawal (Mentor: Vettel): 2nd place undergraduate at ARL Summer Internship Symposium (c.f. ARL-TM-2011).

2. Project 1: WPLI as a Method for Identifying Task-Related Functional Networks in EEG Recordings during a Shooting Task

2.1 Authors

The author on this report is Sandhya Rawal (ARL-TM-2011, 2001). Significant contributors on the project were Jean Vettel (mentor), Samantha Luo, and Kaleb McDowell from ARL/HRED.

2.2 Introduction

EEG records electrical activity from the brain by placing electrodes along the scalp, and the study of this activity through EEG is a prevalent methodology used in neuroscience. EEG has several advantages over other prevalent methodologies, in that it can be used outside of the laboratory and has a high temporal resolution. EEG data have been analyzed at individual electrode sites to identify patterns of brain activity when an event occurs. However, the brain relies on communication between brain regions, so developing analysis methods to investigate brain activity between regions may provide additional information over analyzing electrical activity at single locations. Specifically, identifying the communication between brain regions that occurs during tasks may provide information regarding the cognitive processes involved in the tasks. The brain regions and their connectivity involved in this communication during a task are referred to as the task-related functional network.

One approach to identify task-related functional networks is to investigate the synchronization of neural activity between different brain regions. A common approach calculates statistical interdependencies between electrical activity recorded from pairs of electrodes. Each electrode can capture electrical data from different local regions of the brain, so the interdependencies between two electrodes may suggest neural communication. Although neural communication is fast, occurring in milliseconds, EEG has a high temporal resolution, making it a suitable method for identifying communication among brain regions. However, EEG often has a low signal-to-noise ratio based on movement and muscle artifacts. Another phenomenon that contributes to the low signal-to-noise ratio is often referred to as the volume conduction problem, when two nearby electrodes tend to pick up activity from the same source, giving rise to false correlations between the time series.

To address these problems, Stam and colleagues (2007) introduced a measure called Phase Lag Index (PLI) to address volume conduction issues. PLI is based upon the idea that nonzero phase lag between two time series is not caused by volume conduction from a single source. Therefore, it may capture the communication between brain regions, as these communications have a delay, or a nonzero phase lag, due to axonal transmission properties. The delay exists because brain regions must communicate through a physical biological medium, neurons, and thus cannot

communicate instantly. PLI is less affected by common source problems than the traditional measures of functional connectivity.

However, according to Vinck and colleagues (2011), PLI is limited by the discontinuity of phase lag estimates between zero and infinitesimally small non-zero phase lags. They claimed that both the sensitivity to noise, including volume-conduction, and the capacity to detect changes in phase synchronization is hindered by the discontinuity of PLI. To improve upon PLI, Weighted Phase Lag Index was introduced by Vinck and colleagues. In WPLI, the contribution of the observed phase leads and lags is weighted by the magnitude of the imaginary component of the cross-spectrum. Vinck and colleagues (2011) demonstrated two advantages of WPLI over PLI, reduced sensitivity to noise sources and increased power to detect changes in phase synchronization.

The advantage offered by WPLI of eliminating noise in EEG data is particularly useful for Army purposes because it allows for future studies and product development based on noisy EEG data that would be encountered in real-life situations outside of the laboratory. Artifacts introduced in real-world settings seriously exacerbate the low signal-to-noise ratio, but the ability to identify cognitive activity within the noisy data may allow for discovery of cognitive processes in real-world settings. Identifying nonzero phase lag statistical interdependencies via WPLI may allow for the identification of this cognitive activity.

WPLI, therefore, presents itself as a methodology to provide functional connectivity data in studies performed in real-world conditions. Accordingly, this project applies WPLI analysis to previously collected EEG data from a Marine performing a shooting task. WPLI was computed on epochs of data surrounding the trigger pull event, which consists of both brain activity and movement artifacts from the weapon recoil. This project evaluates the use of WPLI as a method to provide functional connectivity data that identifies task-related cognitive activity not identified using traditional time-frequency analyses.

2.3 Methods or Approach

2.3.1 Participants

In the original study (Kerick et al., 2007), 18 participants volunteered, and 17 of the participants were U.S. Marines and 1 was a U.S. Army Ranger. All had completed basic training and shooting qualifications. The data collected from 1 participant of the 18 was selected for analysis.

2.3.2 EEG Acquisition

The data were previously collected by Kerick et al. (2007). The data were acquired at 500 Hz using a Neuroscan system with 34 active electrodes, including 2 horizontal and 2 vertical eye channels and 2 mastoid reference channels. These analyses use the 28 non-reference electrodes.

2.3.3 Task and Event Extraction

The EEG data analyzed in this report were acquired from the participants during a simulated shooting task. The original study by Kerick and colleagues (2007) involved eight shooting conditions. The conditions included single and dual task conditions in which the Soldier was required to perform only a shooting task or perform a shooting task while performing an arithmetic task; with either short (2–4 s) and long target (4–6 s) exposure and with all enemy targets or mixed enemy and friendly targets (Kerick et al., 2007). However, this report investigates only the condition that had a single task load, all enemy targets, and long target exposure.

The shooting scenarios were a simulation of an outdoor shooting range at Aberdeen Proving Ground, MD, and the rifle provided to the participant was demilitarized to emit a laser beam for fire. The rifle also simulated the recoil that follows an actual shot in order to imitate the type of artifact obtained in a real-world shooting scenario. A digital terminal board sent event markers, including onset and offset times of targets, trigger responses, and target hits and misses, from the simulation system to the EEG recording system. Since all targets were enemy targets, no decision to shoot was necessary. The participant had to search for the enemy target, orient the weapon towards the target, aim, and pull the trigger.

Thirty trials of the event type in which participants aimed and shot successfully were extracted by epoching the data around the event from –3 to 2 s, where 0 s corresponds to the event marker from the digital terminal board, indicating that a shot was fired at the enemy target.

2.3.4 EEG Pre-processing

All pre-processing, including bandpass filtering and some data rejection, was performed and described by Kerick and colleagues (2007). EEGLAB scripts were used to automatically remove bad channels. Independent components (ICs) were obtained from independent component analysis (ICA) decomposition. Those with eye movements or muscle artifacts were removed. The channel data without the eye movement and muscle artifact ICs were then analyzed.

2.3.5 Analysis

WPLI and time-frequency data in 6 frequency bands, delta through gamma, were calculated. The derived WPLI and time-frequency was extracted in the epochs surrounding the trigger pull (–3 s to 2 s). For each electrode (pair) and frequency band, significance was determined by comparing each time point (–3 to 0 s) across all 30 shots to a baseline determined by averaging across the whole data epoch. The significance level was obtained by dividing 0.05 by 501 ($p < 9.98003992 \times 10^{-5}$) to account for the chance occurrence of a significant test (Type I error). To further correct for the Type I error, at least five consecutive time points had to be significant in order to be considered a significant point grouping for WPLI and at least 25 consecutive time points were required for significance in the time-frequency analysis. The requirement for

consecutive time points for significance is based on the estimated time course of communications between brain regions.

2.4 Results and Discussion

WPLI and time-frequency measures were calculated from EEG data acquired from a Soldier during performance of a shooting task. This project attempts to identify task-related functional networks to further understand cognitive processes that occur before the trigger pull; however, the movement artifact caused by the simulated recoil makes the signal-to-noise ratio low. A technique that is impervious to artifacts of this type may allow for identification of cognitive processes occurring concurrently with the movement artifact. In this project, we investigate WPLI to determine if task-related functional networks can be identified after removing the zero phase lag statistical interdependencies between pairs of channels. A traditional time-frequency analysis at individual channel locations is used as a point of comparison.

The channels that were identified as significant in time-frequency data are indeed different from the ones identified in WPLI. Twenty-seven groups of points were significant prior to the trigger pull in the 28 electrodes and 6 frequency bands studied using time-frequency analysis. Fifty-eight groups of points were significant in the 378 electrode pairings in the 6 frequency bands studied using WPLI analysis. In figure 4, the results are plotted on a schematic view of the electrodes on the head, where the front of the brain is located at the top of the graph (Fz). In (a), all electrodes are present and labeled on the figure in red. The Fz electrode is marked by a larger red circle. The significant channels that were identified in time-frequency data are highlighted in black. Figure 4b illustrates the significant channel pairs identified by WPLI with black lines between the independent electrodes. The location of each electrode in (b) is the same as in (a).

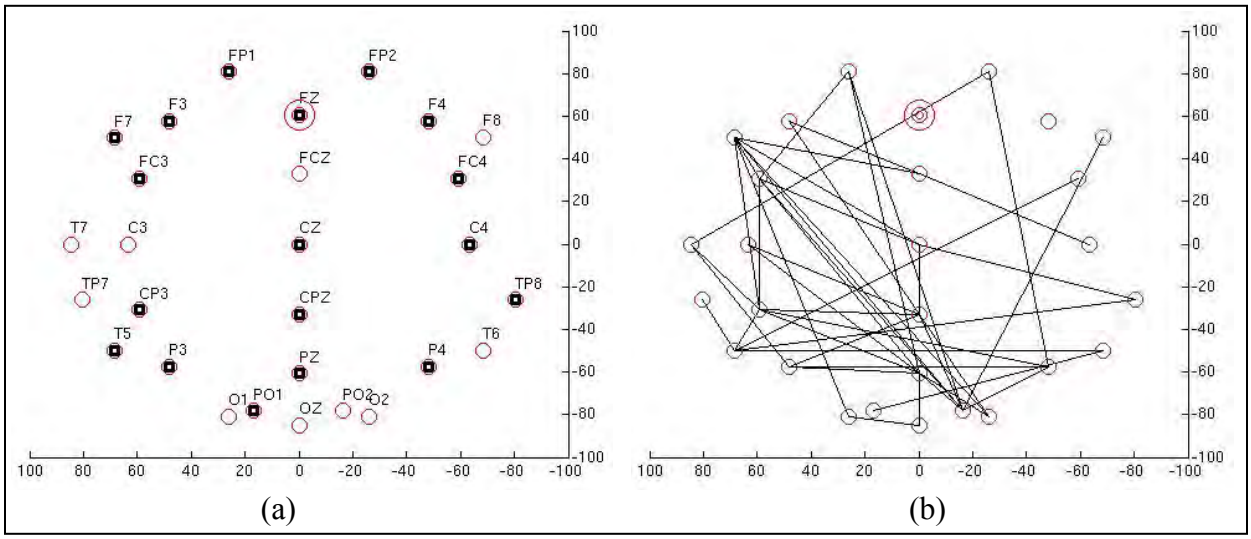

Figure 4. (a) The map of electrodes depicted highlights the electrodes with significance in black. (b) The map of electrodes depicted highlights the nonzero phase lag statistical interdependencies identified by WPLI with black lines between the interdependent electrodes. The location of each electrode is the same as in a.

The differences between figure 4a and b highlight the additional information provided by the WPLI measure. The significance of individual channel locations indicated by the electrodes highlighted in black in figure 4a appears to be distributed symmetrically. However, the distribution in the WPLI analysis in figure 4b is more heavily localized to the left hemisphere. Interestingly, the WPLI analysis reveals a left lateralization of the paired network communication among brain regions, providing an insight not captured in the channel analysis. The involvement of the frontal motor cortex and the parietal cortex suggests that the cognitive activity identified may be motor-spatial planning, as the frontal cortex is involved in planning and in motion and the parietal cortex integrates sensory information from different modalities, particularly for spatial sense. The increased interdependencies in the left hemisphere is consistent with previous literature, as left temporal alpha power is consistently observed in marksmen few seconds before the trigger pull (Kerick et al.).

In addition to the lateralization, the WPLI analysis also revealed activity in the occipital electrodes not found in the channel-based analysis. All occipital electrodes show interaction with the F7 electrode, suggesting communication between the visual cortex and the frontal cortex. This communication may reflect that the shooting task requires planning in response to a visual target before the trigger pull. However, the possibility that communication between the occipital electrodes and the F7 electrode reflect the eye movements occurring near the F7 electrode must be addressed in further research, as this report does not address the potential issue of brain activity correlated to muscle activity.

Figure 4 highlights the promise of WPLI to reveal network communication among brain regions. The plots show all pairs of electrodes that are statistically significant point groupings, but we were also interested in what pairs reveal an extended window of communication during the 3 s before the trigger pull. As a preliminary exploration, we plotted the four longest groups of significant periods, which are illustrated in figure 5. The blue line represents the WPLI waveform and the black lines enclosing the blue line represent the confidence interval.

All four pairs included a frontal and parietal electrode (Fz and CP3, FC3 and Pz, F8 and P02, and C3 and Pz). All waveforms follow a similar downward trend from 3 s before the trigger pull to the trigger pull. However, the first pair (2a), contains a significant point grouping immediately before the trigger pull, while the other three pairs (2b–d) contain significant groupings around 3 s before the trigger pull. Another similarity is the frequency bands in which the significant point groupings occur, as three of the four longest groups occur in the theta (4–8 Hz) band. Figure 5c is the only significant point grouping that occurs in the delta (1–4 Hz) band. Further analyses are needed to clarify the significance of these pairs, although these particular pairs reflect the general pattern of communication between parietal and frontal regions shown in figure 4.

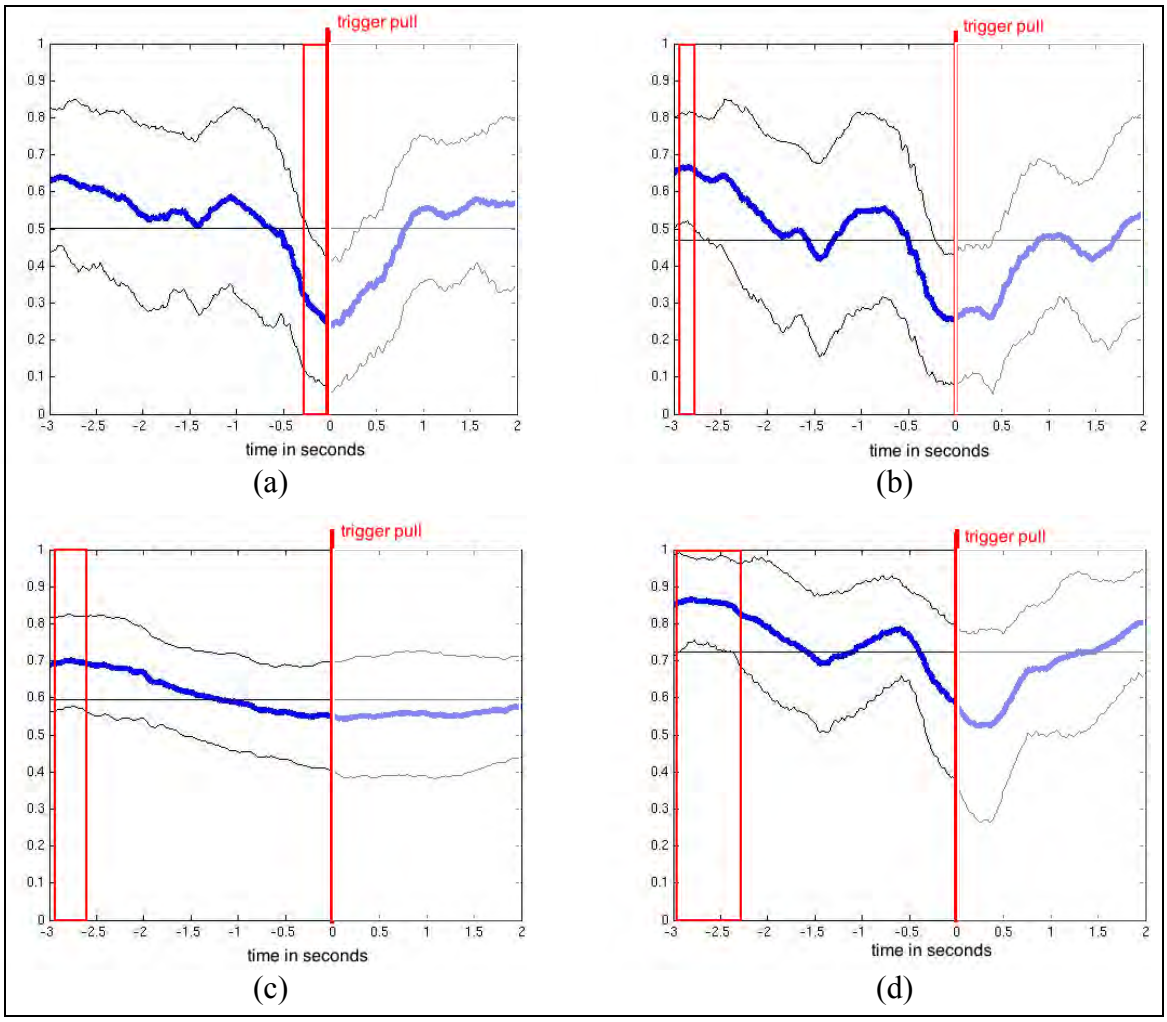

Figure 5. (a) The WPLI analysis depicted was conducted in the theta band, 4–8 Hz, on the Fz and CP3 electrode. Thirty significant points were found from –290 to 0 ms before the trigger pull, (b) the WPLI analysis depicted was conducted in the theta band, 4–8 Hz, on the FC3 and Pz electrode. Thirty significant points were found from –2990 to –2700 ms before the trigger pull, (c) the WPLI analysis depicted was conducted in the delta band, 1–4 Hz, on the F8 and P02 electrode. Thirty-two significant points were found from –2910 to–2600 ms before the trigger pull, and (d) the WPLI analysis depicted was conducted in the theta band, 4–8 Hz, on the C3 and Pz electrode. Sixty-four significant points were found from –2990 to –2360 ms before the trigger pull.

There are several ways to improve on these preliminary results. Primarily, all 18 participants in the study must be analyzed. The patterns observed in the single participant strongly support the extension of these analyses to all participants. Second, the statistical approach may have been suboptimal. As was discussed regarding figure 5, all four waveforms followed a generally similar pattern, yet the statistical approach revealed significance at different times relative to the trigger pull. Alternative approaches conducted in all 18 participants may reveal a clearer result. Finally, this report does not address the potential issue of brain activity that is correlated to muscle activity, which may be the case for the activity of the F7 electrode due to the electrode's proximity to the eye. However, further research is necessary.

2.5 Conclusions

WPLI analysis suggests that the measure may be able to capture task-related functional networks during cognitive tasks, even in the midst of large-scale movement artifacts. Further research looking across more individuals and at more tasks is needed to provide more definitive results. However, the results from this one participant support that conducting pair-wise electrode analysis in addition to individual electrode analysis may provide more information than individual electrode analysis alone. While EEG time-frequency reveals a symmetric distribution of electrodes with significance, WPLI analysis finds statistical interdependencies more heavily lateralized to the left hemisphere. In addition, WPLI reveals communication with occipital electrodes, whereas these individual channels are not marked significant in the time-frequency analysis. The preliminary findings reported here suggest that the F7 electrode may be a hub of communication, with several significant pairings with other electrodes. Therefore, the methodology used in this project shows that WPLI may provide functional connectivity data not accessible in time-frequency data. WPLI provides an interesting method for investigating how the brain performs cognitive tasks even with large artifacts in the signal, allowing for further investigation and understanding of Army tasks performed in complex environments.

3. Project 2: Functional Connectivity of EEG Data Using the Weighted Phase Lag Index (WPLI): Robustness to Artifacts in Real-world Environments

3.1 Authors

The authors on this project are Scott Kerick from ARL/HRED, Manuel Vindiola from Dynamics Research Corporation (DRC), and Kaleb McDowell from ARL/HRED.

3.2 Introduction

Ecological psychologists have long known that human behavior cannot be understood independent of the complexity that the real-world imposes and that it is critical to study human behavior within context (Gibson, 1977; 1979). As researchers have attempted to comprehend the relationship between brain function and behavior, similar arguments have been made stressing the importance of understanding brain function within naturalistic environments (Gevins, et al., 1995; Makeig et al., 2009; Oie and McDowell, 2011; Parasuraman, 2003; Parasuraman and Rizzo, 2007). Some have gone as far as proposing the idea that laboratory-based studies isolated from real-world experience may generate fundamental misunderstandings of the underlying principles being investigated (cf., Kingstone et al., 2008). It would thus seem important to conduct neuroscience investigations in natural settings to address these concerns. However, the dominant brain imaging methods of the day require participants to lie or sit completely still within large chambered machines (fMRI) or under a hood (MEG), which imposes a substantially

different environment than that experienced by humans performing tasks in natural settings. This brings into question the external validity and generalizability of much of neuroimaging research (Kingstone, Smilek, and Eastwood, 2008; Kingstone et al., 2003). Recent findings have bolstered these arguments by demonstrating the importance of context in the differential engagement of neural resources during task performance (Foerde et al., 2006), and further stressed that to better understand how the human brain operates in the real world, considerably more research is needed to investigate the potentially important differences between the brain function and behavior observed in simplistic and controlled laboratory environments and that observed in complex and real-world settings.

One of the many reasons that more neuroscience has not been conducted in real-world settings is the challenge of recording quality signals from the brain in natural environments. Part of this challenge is due to the characteristics of the technologies available for the purpose—many of which are not suitable for recording brain dynamics in real-world environments. At present, the only two brain imaging technologies that are portable and wearable and thus capable of recording brain dynamics as participants interact relatively freely in the naturalistic environments are EEG and functional near-infrared spectroscopy (fNIR). While fNIR is a relatively new technology, EEG has been around since the 1920s (Berger, 1929) and over the past five years, there has been a dramatic increase in commercially available and prototype mobile EEG systems (Lin et al., 2010). Both technologies provide potentially useful, yet different, indices of brain activity. fNIR provides a measure of changes in blood oxygen concentrations and blood volume in response to activity of neurons (Izzetoglu et al., 2007), whereas EEG measures fluctuations in electrical fields generated by the net electrochemical activity of populations of pyramidal cortical neurons and inter-neurons (Nunez and Srinivasan, 2006). While both of these imaging modalities can provide relatively high quality signals in highly controlled settings, they both have very low signal-to-noise ratios in real-world settings due to large artifacts that can be induced by biological and non-biological sources.

In addition to the methodological challenges of obtaining high quality brain imaging data from participants in natural environments, another major challenge is to analyze and interpret brain function within these environments. The brain is a complicated network of neural elements that has been argued to function in order to meet two diverse requirements: the local specialization of neurons for processing specific types of information and the integration of information across a more global systems level (Friston, 1994; Rubinov and Sporns, 2010; Sporns, Tononi, and Edelman, 2000). While much work has focused on the local specialization of neural assemblies, it has been argued that additional focus on the systems level is required in order to advance our current understanding of brain dynamics (Borner, Sanyal, and Vespignani, 2007; Le van Quyen, 2003; Varela et al., 2001). Network approaches, and specifically, the inferences of functional connectivity upon which these approaches, in large part, are built, and they offer a potential approach towards such a systems view. However, significant issues have been identified for deriving functional connectivity from EEG data in particular. Of primary concern for EEG-based

methods are issues associated with volume conduction and the use of active reference electrodes, both of which cause an artificial inflation of measures of association between pairs of electrodes (Bullmore and Bassett, 2010; Stam, Nolte, and Daffertshofer, 2007). In an attempt to address the joint problems of volume conduction and common source distribution at the scalp, Stam et al. (2007) introduced the PLI as a novel means of indexing the interdependencies among multichannel EEG data. More specifically, the use of the PLI is "… based upon the idea that the existence of a consistent, nonzero phase lag between two times series cannot be explained by volume conduction from a single strong source and, therefore, renders true interactions between the underlying systems rather likely" (Stam et al., 2007, p. 1179). Using simulated and actual EEG and MEG data, Stam et al. (2007) demonstrated that PLI is less affected by volume conduction and common sources than are traditional measures of functional connectivity such as phase coherence and the imaginary component of coherence. However, a limitation of PLI is the discontinuity of phase lag estimates between zero and infinitesimally small non-zero phase lags. To address this concern, Vinck et al. (2011) introduced the WPLI, which weights the observed phase leads and lags by the magnitude of the imaginary component of the cross-spectrum. As Vinck et al. (2011) demonstrated, WPLI exhibited reduced sensitivity to uncorrelated noise sources and, concomitantly, increased statistical power for detecting phase synchronization as compared with PLI. They further argue that because WPLI is based on the imaginary part of the cross-spectrum, it is generally decreased, not increased with the addition of noise. Although PLI and WPLI have been tested using simulated data (controlled, known-truth) and on data from patients experiencing epileptic seizures (a condition exhibiting drastic brain synchronization detectable using various methods), there exists a need to validate these phase synchronization approaches on noisy data recorded in operational environments. Such validation could lead to the identification of a measure of functional brain dynamics that is sensitive to phase synchronization of brain source signals but resilient to artifacts and would open the door to network analyses and other systems-level approaches to understanding brain function within complex, naturalistic environments.

3.2.1 Objective

In response to the challenges presented above and the potential of WPLI to become a core measure for research in complex, artifact-inducing environments, we aim to further understand WPLI with respect to noise levels on the scale of real-world artifacts. To accomplish this objective, we examine EEG recorded from participants shooting at pop-up targets in a simulated environment with realistic weapons including requirements for dynamic movements and recoil immediately following weapon triggering. From these data, WPLI was derived and examined on data epochs consisting of three types of events: non-event locked artifacts (i.e., primarily non-brain activity), non-event locked alpha bursts (i.e., primarily brain activity), and trigger-locked activity (i.e., a mix of brain activity and artifact induced by recoil). Similar to previous efforts, the measures of functional connectivity were derived among all pair-wise combinations of electrodes.

3.3 Methods or Approach

3.3.1 Participants

Seventeen male U.S. Marines and one U.S. Army Ranger volunteered as participants (mean age 19.8 ±4.2). All had completed basic training and shooting qualification (8 marksmen, 5 sharpshooters, 5 experts). All but one of the participants was right-hand and right-eye dominant; one participant was left-hand and left-eye dominant. The voluntary, fully informed consent of the persons used in this research was obtained as required by 32 CFR 219 (1999) and AR 70–25 (1990). As is described below, data for this analysis were selected from 12 of these original 18 participants.

3.3.2 Task and Event Extraction

The EEG data analyzed in this report were acquired from participants during performance of eight different simulated threat-engagement shooting tasks, an arithmetic task, and two resting tasks (for more details, see Kerick et al., 2007). For this methodological paper, we visually inspected and manually selected three types of transient events (200–2000 ms duration) from the continuous EEG data: (1) non-event-related movement artifacts ("Random"), (2) spontaneous alpha bursting ("Alpha Bursts"), and (3) event-related brain activity with artifacts ("Trigger"). Random artifacts were primarily muscle artifacts due to shifting positions between trials, spontaneous alpha bursting events were selected based on the onset of clearly visible alpha oscillatory patterns observable across multiple channels, and event-related brain activity with artifacts were selected based on existing trigger event markers in the data, which were always immediately followed by weapon recoil and mechanical/movement artifacts. Figure 6 shows an example event of each type within continuous EEG recordings. Fifty trials of each event type were extracted by epoching the data around each event from –1 s to 2 s, where 0 s corresponded to the onset of artifact contamination for Random events, the onset of alpha oscillations for Alpha Bursting events and the time of the trigger pull for the Trigger events. The 150 total selected events were sampled from 12 of the participants and 10 of the conditions.

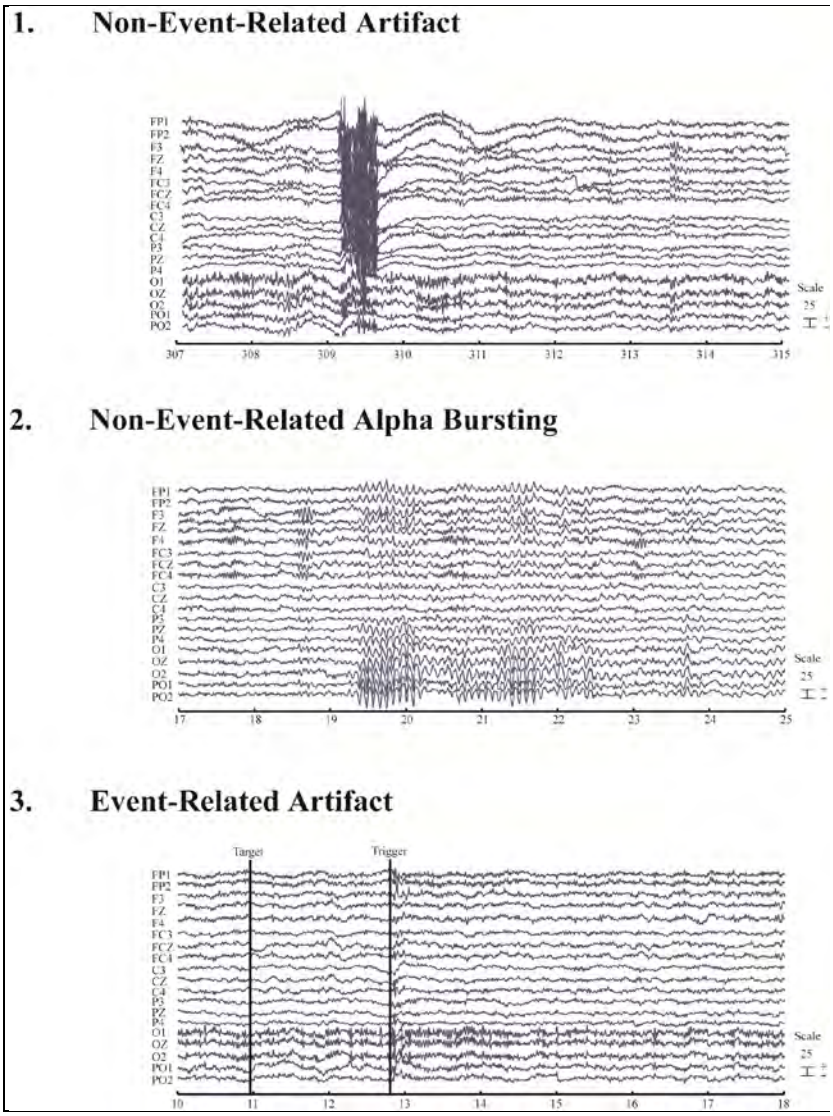

Figure 6. Example illustrating three types of events extracted from continuous EEG channel data. (Top to bottom): (1) non-event-related artifact, (2) transient alpha bursting, and (3) event-related artifact. Note that these signals are from data prior to epoching and that a longer than 3 s time window is illustrated.

3.3.3 EEG Acquisition

EEG data were acquired at 500 Hz using a Neuroscan system (NuAmps 40-channel) with 34 active electrodes, 2 horizontal and 2 vertical eye channels, and 2 mastoid reference channels (left and right). The right mastoid served as a common reference for all other channels during online recording. Online filter settings were DC-100 Hz.

3.3.4 EEG Pre-processing

All pre-processing was executed using EEGLAB (ver. 9.0.2.2b; Delorme and Makeig, 2004) running on Matlab (2008a) installed on a 64-bit Linux operating system. Raw continuous EEG data from each condition were bandpass filtered from 1–50 Hz using a two-way least-squares

finite impulse response (FIR) filter (using EEGLAB function *eegfilt.m*). After bandpass filtering the data, files for each subject and condition were saved for use in two separate data processing streams. For the first processing stream, data were concatenated from each of the 11 conditions for each subject separately and then epoched into non-overlapping 500-ms windows. Bad channels were identified and removed from the filtered, concatenated, epoched data, by visual inspection aided by automatic channel-rejection procedures based on kurtosis and joint probability functions (using EEGLAB function *pop_rejchan.m*). Once bad channels were removed, automatic artifact-detection procedures were applied (using EEGLAB function *pop_rejmenu.m*) based on thresholds for kurtosis, joint probability, abnormal distribution, and abnormal trends, as well as visual inspection to remove any epochs consisting of non-stereotypical transient artifacts (e.g., gross muscle contamination, cable sway artifacts, etc.). The filtered, artifact-reduced, concatenated, epoched data (i.e., "clean EEG") were then re-referenced to an average reference derived from all active channels (excluding eye channels). The rationale for concatenating data across all conditions and removing non-stereotypical artifacts was to provide the cleanest and greatest amount of data available for ICA decomposition (Onton and Makeig, 2006). Extended infomax ICA (Bell and Sejnowski, 1995; Makeig, Bell, Jung, and Sejnowski, 1996) was then applied to decompose the clean EEG data into spatially fixed, maximally temporally independent components (using EEGLAB function *runica.m*) and dipole models were fit to each of the independent components (ICs; using EEGLAB plug-in *DipFit2.2*). ICs were then classified into three categories based on dipole source models, topographic maps, spectra and activation waveforms: (1) clearly brain-source, (2) clearly artifact-source (these IC reflected primarily eye blinks and muscle artifacts), and (3) mixed-source. However, while the ICs derived using these methods can be used to separate brain-source from artifact-source under good conditions, large transient artifacts permeate nearly all ICs. The outputs from the ICA decomposition (IC weights, inverse weights, sphering matrix, component indexes and IC classifications) and dipole source models were then saved.

For the second processing stream, we retrieved, for each participant, each of the band-pass-filtered (1–50 Hz) data files from each of the 11 conditions and removed the same bad channels removed in the first processing stream and then re-referenced to the average of all remaining good channels (however, the previously identified bad epochs were not removed). The outputs from the ICA decomposition and dipole source models were then copied into the data structures for each participant and each of the 11 conditions. ICs classified as artifact-source were removed and the EEG data were then back-projected to channels void of those ICs resembling artifacts (Jung et al., 2000; Onton et al., 2006) (i.e., "ICA-filtered EEG data"). Note that we did not remove any of the transient, non-stereotypical artifacts in any of the 11 condition data sets, beyond those that were removed by ICA decomposition (e.g., eye-blinks [ICs 1, 2, 5, 10] and some muscle artifacts [ICs 21 and 22]; see figure 7) as the purpose of this study was to observe the effects of such artifacts on WPLI.

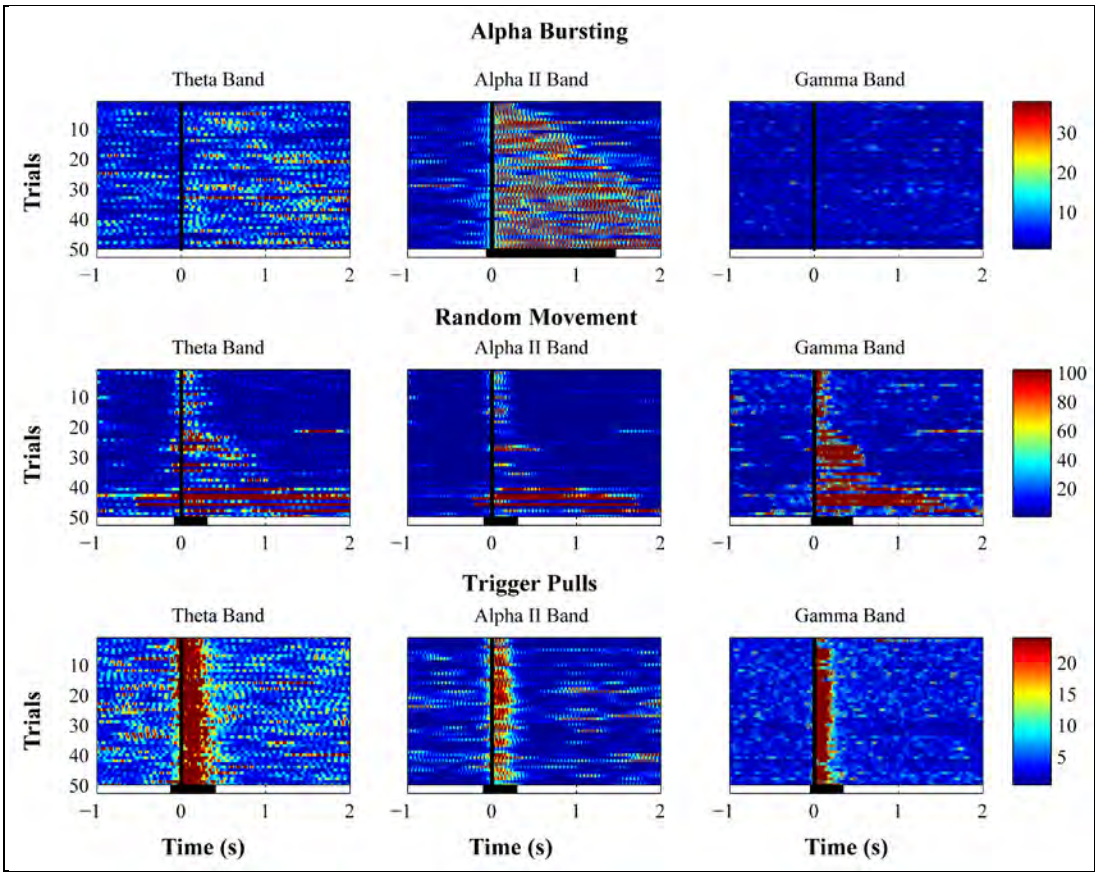

Figure 7. Channel power by event and frequency band for each of the 50 individual trials. Within each plots, trials are sorted by the length of the EEG event (shorter events on top). Three of the six frequency bands (theta, alpha II, gamma) are plotted in columns. All three event types (Random, Alpha, and Trigger) are plotted in rows. A black bar below each plot shows when the distributions of power values were significantly higher than baseline (–1 0 s).

3.3.5 Weighted Phase Lag Index (WPLI)

WPLI was derived from the continuous ICA-filtered EEG channel data for each participant in each condition. WPLI was derived for each pair-wise combination of channel data. Below we describe how WPLI was derived. Data were first band-pass filtered using a 4th order Butterworth filter at the following frequency bands: delta (1–4 Hz), theta (4–8 Hz), alpha I (8–10 Hz), alpha II (10–13 Hz), beta (13–30 Hz), and gamma (30–45 Hz). The Hilbert transform was then applied to each of the band-pass filtered data to obtain an analytical signal. WPLI is defined as follows:

$$WPLI = \frac{|E\{\Im\{X\}\}|}{E\{|\Im\{X\}|\}} \quad (1)$$

where $\Im\{X\}$ is the imaginary part of the cross-spectrum (Vinck et al., 2011). WPLI estimates were computed over four cycles for each frequency band (i.e., varying length windows were defined as four times the length of one cycle of the lower bound of the band-pass filter and were stepped in 10 ms increments [five samples] for each frequency band).

For each signal type (spectral band power, WPLI), event type (Random, Alpha Burst, Trigger), and band-pass filter setting (delta through gamma), separate significance tests were conducted using the Wilcoxon rank sum test for equal across-trial distributions between pre-event data and each time step through the entire length of the trial. That is, for each of the 36 possible time series, 301 (time points from [–1 2]) rank sum tests were performed comparing distributions between the pre-event data (100 time points by 50 trials) and each specific time point (1 time point by 50 trials). Significance was determined using Bonferroni corrections ($p < 2.3 \times 10^{6}$) to account for the chance occurrence that any of the several tests were significant. In addition, at least five consecutive time points had to be significant in order to be included in the results. Note that PLI measures were also computed for each bandpass filter setting and for each condition. As nearly identical results were observed between WPLI and PLI, only WPLI will be reported.

3.4 Results and Discussion

The challenge of recording quality brain signals in complex, real-world environments is a significant obstacle to neuroscience and related fields. Here, we examine a novel measure of functional brain connectivity (i.e., WPLI [Vinck et al., 2011]) that shows promise for being a robust measure of brain communication in the face of real-world, non-brain artifacts. In order to assess the robustness of WPLI to realistic, real-world artifact contamination of EEG recordings, three types of events representing non-brain artifact, brain activity, and a mix of non-brain artifact and brain activity were examined. To confirm the severity of the artifact, advanced signal processing of the EEG data (i.e., ICA; Makeig, Bell, Jung, and Sejnowski, 1996) was performed that, under typical laboratory conditions, can isolate brain-sources from non-brain sources. Both non-brain artifact (Random) and mixed (Trigger) events were selected for which the artifact overpowered the source discrimination. We argue here that the results support that WPLI is insensitive to large non-brain artifacts and appears to be sensitive to brain activity.

3.4.1 Spectral Power

Figure 7 illustrates the spectral power for individual trials in the channel data, respectively, for three frequency bands. The black bars below the individual-trial plots in figure 7 as well as the information in table 1 indicate the time points that are significantly higher than baseline [–1 0 s].

Table 1. Latency ranges (low–high ms) of significant power increase for each event type and frequency band.

	Delta	**Theta**	**Alpha I**	**Alpha II**	**Beta**	**Gamma**
Random	–10:160 180:260	–80:300	–80:320	–90:300	–20:400	–30–450
Alpha	–	–	–30:1590	–60:1460	160:350	–
Trigger	–140:330	–120:400	–140:680	–100:290	–60:310	–40:340

Random

The channel data exhibited significant ($p < 2.3 \times 10^{6}$) power increases relative to baseline in each of the six frequency bands. These significant increases occurred from 90 to 10 ms prior to onset and extended for 260 to 450 ms after event onset (see table 1). The data indicate a high level of broadband power (e.g., compare scales across all three event types), which is consistent with artifact. While significant power increases across all six frequency bands existed, on a trial-by-trial basis power increases following event onset appear to be less variable in the higher frequency bands, which is also consistent with muscle-generated artifact that generally has more power at the higher end of the EEG spectrum.

Alpha Bursting

The channel data exhibited significant ($p < 2.3 \times 10^{6}$) power increases relative to baseline in the two alpha bands and the beta band. The significant increases generally occurred from –60 to –20 ms prior to onset and extended for 350 to 1590 ms after event onset (see table 1). Overall, the data indicate higher pre- and post-event power in lower frequency bands (e.g., compare apparently random power increases in theta to very low power in gamma), which is consistent with cortically-generated activity. On a trial-by-trial basis, the power distribution across frequency bands appears to have similar variability. These results demonstrate the properties of neurally-generated signal without substantial artifact.

Trigger

The data show significant ($p < 2.3 \times 10^{6}$) power increases relative to baseline in each of the six frequency bands. These significant increases occurred from –180 to –40 ms prior to onset and extended for 330 to 500 ms after event onset (see table 1). In this event, brain activity had to occur prior to the trigger pull. The relatively early onsets of the power increases occurred well before the recoil (i.e., large movement artifacts), and this timeframe supports the interpretation that the brain activity was, in part, contributing the power in this event. The data also indicate similar broadband power levels as those observed for the alpha bursting trials (e.g., compare scales) and indicate similar temporal patterns of power distribution across frequency bands. We interpret the relatively similar levels of power across frequencies to reflect a combination of both the lower frequency dominance that is typical of brain activity combined with the higher frequency dominance that is typical of muscle-generated artifact. On a trial-by-trial basis, the post-event power increases around trigger onset appear very consistent across frequency bands, which may reflect the consistency in both brain activity and recoil artifacts associated with a trigger pull.

3.4.2 Weighted Phase Lag Index

In discussing the WPLI results, we need to consider several points. First, WPLI is a phase-based measure that generally will only decrease when artifact is evident in the signal (Vinck et al., 2011). Second, here we examined averaged WPLIs, which should enable the ability to detect a

signal decrease associated with large artifacts; however, at the same time it will limit the ability to uncover the characteristics of complex brain-generated network activity (which we leave for future efforts). Third, the windowing to compute the WPLI smears the signal across time, which makes it critical to not only consider the timing of WPLI effects relative to brain/non-brain activity, but also if the effects are asymmetrical to that activity.

Figure 8 illustrates WPLI for individual trials for three frequency bands, respectively. The red bars below the individual-trial plots in figure 8 as well as the information in table 2 indicate the time points for which WPLI is significantly different than baseline [–1 0 s]. Black bars are also included below each individual-trial plot to reference significant time periods observed for the spectral power.

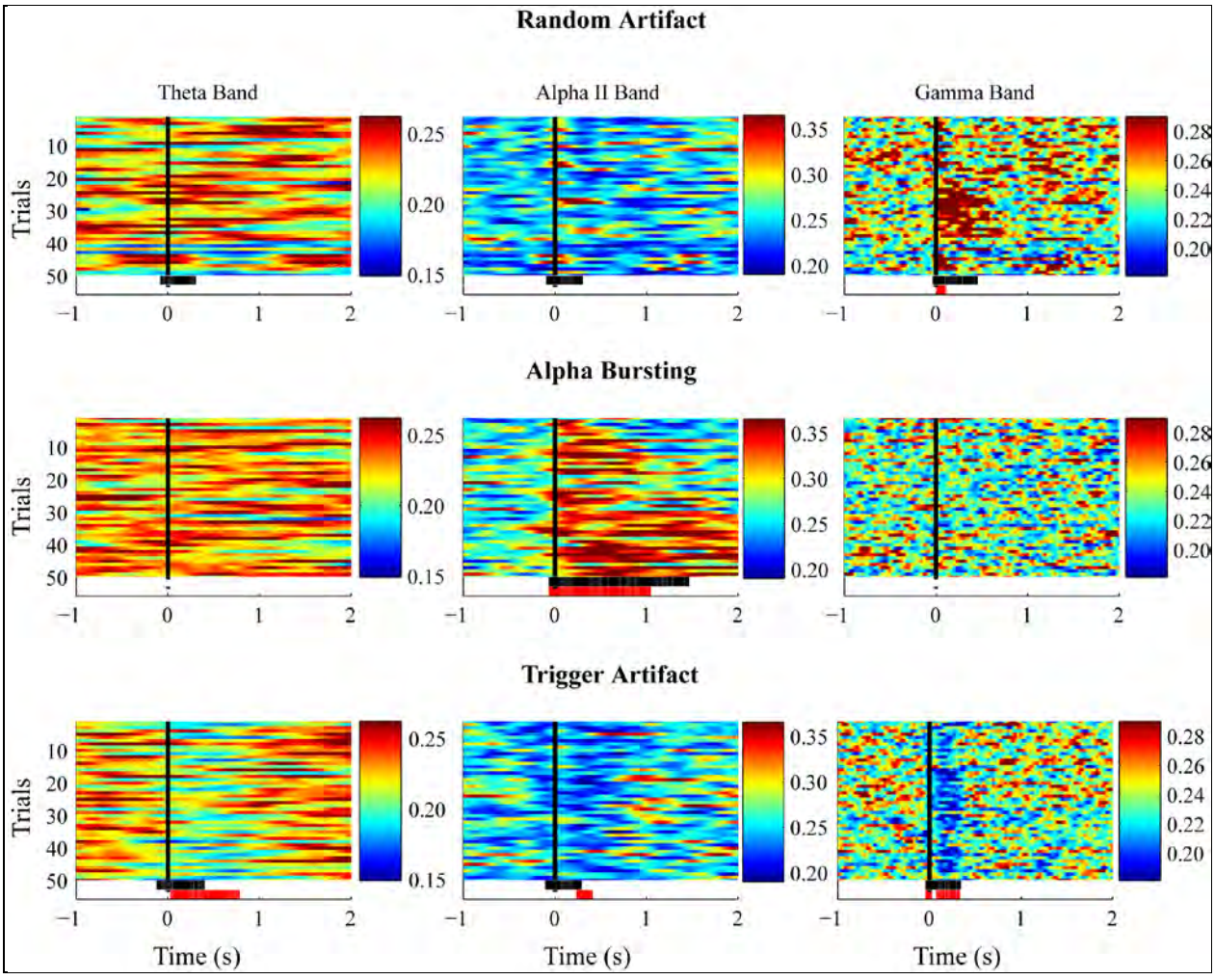

Figure 8. WPLI by event and frequency band for each of the 50 individual trials. Within each plot, trials are sorted by the length of the EEG event (shorter events on top). Three of the six frequency bands (theta, alpha II, gamma) are plotted in columns. All three event types (Random, Alpha, and Trigger) are plotted in rows. A black bar below each plot shows when the distributions of power values were significantly higher than baseline [–1 0 s]. A red bar below each plot shows when the distributions of WPLI were significantly higher than baseline [–1 0 s].

Table 2. Latency ranges (low–high ms) of significant WPLI increase for each event type and frequency band.

	Delta	**Theta**	**Alpha I**	**Alpha II**	**Beta**	**Gamma**
Random	–	–	–	–	–	10:110
Alpha	–	–	–50:960 1300–1650	–60:1040	–	–
Trigger	–	30:780	180:680	240:410	-90:340	–40:20 80:330

Random

The EEG data revealed a significant ($p < 2.3 \times 10^{6}$) increase in WPLI in the gamma band only. The significant WPLI increase began 10 ms after event onset and extended for 110 ms (see table 2). Both in the time period of significance and on a trial-by-trial basis, WPLI does not appear to reflect the artifact-related power increases (e.g., compare duration of significance in the EEG channel data gamma band for power [black bar] and WPLI [red bar]). Further, the short periods of WPLI change are increasing not decreasing as would be expected due to noise artifact. It is conceivable that the WPLI changes are actually reflecting some level of neural activity that could be associated with muscle activity, even though this activity was not "event-locked" to a cognitive activity (e.g., see trigger pull). Importantly, however, the results here illustrate very small changes, especially when considering the amplitude of the artifact and the strength of the results in the following two event types.

Alpha Bursts

The EEG channel data revealed a significant ($p < 2.3 \times 10^{6}$) increase in WPLI in the alpha I and II bands only. In the EEG channel data, the significant increases occurred 60 ms (alpha I) and 50 ms (alpha II) prior to event onset and extended for 940 ms (alpha I) and 1040 ms (alpha II) after event onset; there was also a later period of significance in the alpha I band (see table 2). These data support that WPLI is capable of reflecting brain-based functional connectivity. Further, both in the time periods of significance and on a trial-by-trial basis, the WPLI values of the channel data do not precisely coincide with the brain-related alpha power increases (e.g., compare duration of significance in the EEG channel data alpha II band for power [black bar] and WPLI [red bar]). While supporting that WPLI reflects functional connectivity in this case, these data also suggest a level of independence between amplitude generation and synchronized global activity which has been previously supported (Makeig 2002; 2003).

Trigger

The EEG channel data revealed a significant ($p < 2.3 \times 10^{6}$) decrease in WPLI in all frequency bands except delta. The significant decreases generally occurred 90 to 40 ms before trigger pull in the higher frequency bands (beta and gamma) and 30 to 240 ms after the trigger pull in middle

frequency bands (theta, alpha I and alpha II) and extended for 330 to 780 ms after the trigger pull. These results, particularly taken together with that of the Random and Alpha Burst events, suggest that the WPLI significances are not reflecting muscle-generated artifact: the level of significance for the trigger events are substantially longer and across broader frequencies than that of the random artifact events even though the artifacts were much smaller, and there exists large asymmetrical discrepancies in time period between the channel WPLI and the channel spectral data. Again while supporting that WPLI reflects functional connectivity in the Trigger events, the data also suggest some independence between amplitude generation and synchronized phase activity (Makeig 2002; 2003).

3.5 Conclusions

In summary, we have presented a computational approach that addresses some of the many issues and challenges associated with acquiring and interpreting brain imaging data in the form of EEG signals recorded in an operationally-relevant, non-traditional laboratory environment. Namely, we applied a novel measure of functional brain connectivity based on phase synchronization (i.e., WPLI [Vinck et al., 2011]) among multiple recording sites to investigate the performance of this measure in the face of volume-conducted-artifacts in EEG signals, which present a pervasive problem for translational neuroscience research and understanding brain function in real-world environments. Together, the identification of a measure of functional brain dynamics that is sensitive to phase synchronization of brain source signals but resilient to artifacts would potentially provide important new insights into how the brain functions in complex, real-world settings. That is, the novel WPLI measure appears simultaneously largely insensitive to the large artifacts found in realistic, real-world environments and sensitive to brain-generated functional connectivity. These properties support that WPLI has a strong potential to become not only a core measure for research into understanding brain function in complex, artifact-inducing environments, but may also become a core component in the development of brain-computer interaction technologies. However, before the potential of WPLI can be fully realized, a substantial amount of future research is necessary to uncover the specific sensitivities of WPLI to brain dynamics.

---

4. Project 3: Validating Functional Connectivity Measures Using Neural Mass Models

---

4.1 Authors

The authors on this project are Manuel Vindiola from DRC, Stephen Gordon from DCS Corporation, Jean Vettel from ARL/HRED, and Kaleb McDowell from ARL/HRED.

4.2 Introduction

The human brain can be conceived of as a massively parallel, massively distributed set of electrochemical processors called neurons interconnected with one another by axons. Collectively, trillions of neurons and billions of axons form a complex information processing network. The combined activity and communication of these neurons underlie human cognition and behavior.

When observed individually, each neuron fires according to a non-stationary, random Poisson point process; however, when a population of neurons is combined, their average firing rates form a continuous, periodic, oscillatory pattern of neuronal activity. Oscillatory neural activity has been identified in numerous brain functions including attention, navigation, perceptual binding, and memory (Gray et al., 1989). Oscillatory brain rhythms can be phase-coupled across distant brain regions. Two regions are phase-coupled or phase-synchronized when they display a systematic phase-offset. Phase synchronization has been identified as a way to create a flexible communication structure between distant brain regions (Engel et al., 2005; Fries, 2005).

Communication among brain regions form networks of brain activity, creating stable brain states that capture a global level of neural processing thought to subserve ongoing task demands and behavioral performance. Task-relevant brain networks dynamically reconfigure, capturing the temporal dynamics of the task. These ongoing network reconfigurations may engage different brain regions, alter the nature of the communication between regions, etc. In order to measure and understand the nature of these ongoing brain dynamics, neuroimaging analysis methods have been developed to capture communication between pairs of recorded brain signals.

EEG is a method of measuring electrical activity on the scalp, and evidence suggests that EEG signals preserve the oscillatory characteristics of the firing patterns in the neural regions that generate them. Computational and statistical advancements over the last decade have led to the development of a number of functional connectivity measures that can be applied to EEG signals. There are several classes of connectivity measures, including ones based on correlation, auto-regression, and phase synchronization. In this analysis, we focus on three undirected, phase-based functional connectivity measures that have been designed to identify pair-wise phase synchronizations among separate EEG signals: imaginary component of Coherence (ImC) (Nolte et al., 2004), debiased Weighted Phase Locking Index (dWPLI) (Vinck et al., 2011), and phase-locking value (PLV) (Lachaux et al., 1999). These three methods were chosen because they offer three different views into an issue that typically confounds connectivity analysis in EEG data—volume conduction.

Volume conduction has two major components: (1) brain sources that are mixed together as they pass through the scalp, and (2) artifact sources on the scalp (e.g., eye movements, muscle contractions). In typical analyses of brain function, the aim is to separate artifact from brain and unmix the brain sources. These three measures show different sensitivities to these sources of volume conduction. In general, PLV is negatively affected by both brain and artifact sources of

volume conduction, while both ImC and dWPLI minimize the effect of artifact sources by requiring that the two signals have a systematic phase relationship that occurs at a temporal delay. If the two channels are instantaneously in phase, then ImC and dWPLI both return low functional connectivity values, under the premise that removing zero-phase volume conducted noise signals improves the functional connectivity analysis even if some real communications between brain regions are sacrificed. ImC will also return a low connectivity value for phase-lagged synchronizations if the brain signals and non-brain artifacts induce large amplitudes in the signal. Unlike ImC and dWPLI, PLV returns high functionally connectivity values so long as the two signals are phase-synchronized and the delay is consistent. Since we know volume conduction introduces a linear mixing of the signals, i.e., instantaneous phase synchronization, it is worth examining whether the methods that attempt to deal with this effect perform equally well, or better, in the more ideal, unmixed case. Are these functional connectivity measures able to detect task-relevant changes in ongoing brain network dynamics? To address this question, we applied these functional connectivity measures to simulated oscillatory signals generated by a pair of coupled regions in a neural mass model in order to evaluate how well the measures detected changes in ongoing brain network dynamics when volume conduction was not present. If the measures can detect task-relevant brain dynamics, they provide a critical capability to measure and monitor brain function in Army-relevant tasks and settings and thus open an avenue for neurotechnology development to improve Soldier-system performance.

4.2.1 Objective

In this project, a simulation was developed to validate the functional connectivity measures; that is, can the measure recover the network dynamics when temporal dynamics of phase synchronizations are known to exist? Here, we have a neural mass model with several regions. Each region is parameterized to oscillate with a specific frequency distribution and is coupled with other regions to form a network. We begin with the simplest case of two regions with each region oscillating with one of two possible frequency distributions connected to each other with one of two possible network configurations. We first confirm that the simulated regions generate the oscillatory signals expected from a given network, and then we run each of the three phase connectivity measures to evaluate what network dynamics are captured.

4.3 Methods or Approach

4.3.1 Neural Mass Models

The neural mass models (NMMs) were constructed according to David and Friston's (2003) description. Each region within the NMM is designed to reproduce a time signal with amplitude and oscillation frequencies similar to those observed in local field potential (LFP) recordings obtained by measuring the combined post synaptic potential of hundreds to thousands of real neurons in a cortical column. A key component of these NMMs that makes them suitable for this study is that both the signal patterns they produce and those observed in EEG recordings are oscillatory. A sample signal from a region in a NMM is presented in figure 9.

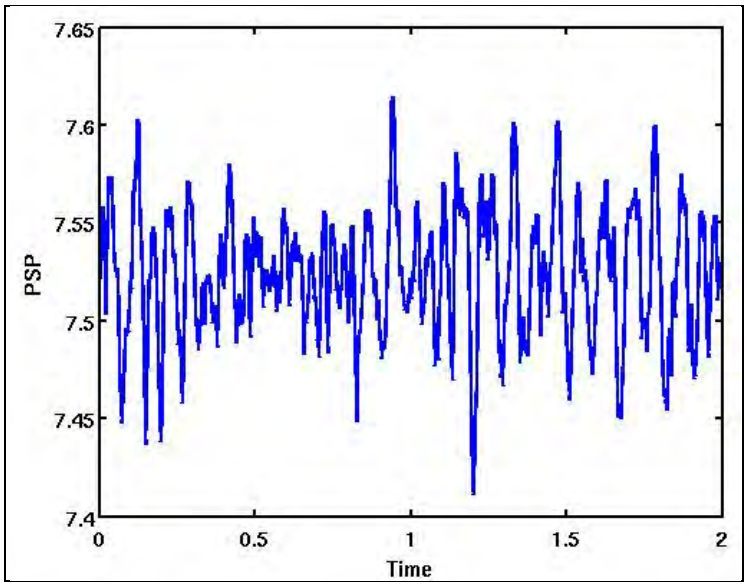

Figure 9. The time course of a single region in a NMM in isolation with two internal subpopulations. The output is generated by nonlinearly combining a weighted mixture of 80% from a subpopulation oscillating at 11 Hz and 20% from a subpopulation oscillating at 43 Hz.

A NMM region is composed of a number of internal subpopulations, where each subpopulation is parameterized to oscillate at one specific frequency. The output signal of a neural mass region is constructed by computing a nonlinear sigmoid transformation over a linear weighted combination of each of the subpopulations. The subpopulations create oscillatory patterns through the interaction of excitatory and inhibitory components of the subpopulation. Each subpopulation, which is loosely based on the structural organization of cortical macro-columns, contains three layers: a pyramidal layer, an excitatory spiny stellate layer, and an inhibitory interneuron layer. The cortical output is modeled by a summed weighting of all the excitatory pyramidal layers. The pyramidal layer receives input from the excitatory spiny stellate and inhibitory interneuron layers of the region. The excitatory spiny stellate layer receives input from the pyramidal layers of other neural mass regions that are part of the same functional network (neighbors), external subcortical bottom-up inputs modeled by a stochastic Gaussian process, and feedback from the pyramidal layers of the same region. The inhibitory interneuron layer receives excitatory feedback input from the pyramidal layers of the same region, and it sends inhibitory output to these same pyramidal layers. Figure 10 depicts a schematic representation of the connectivity among the three parts of a subpopulation and the connectivity between two different neural mass regions.

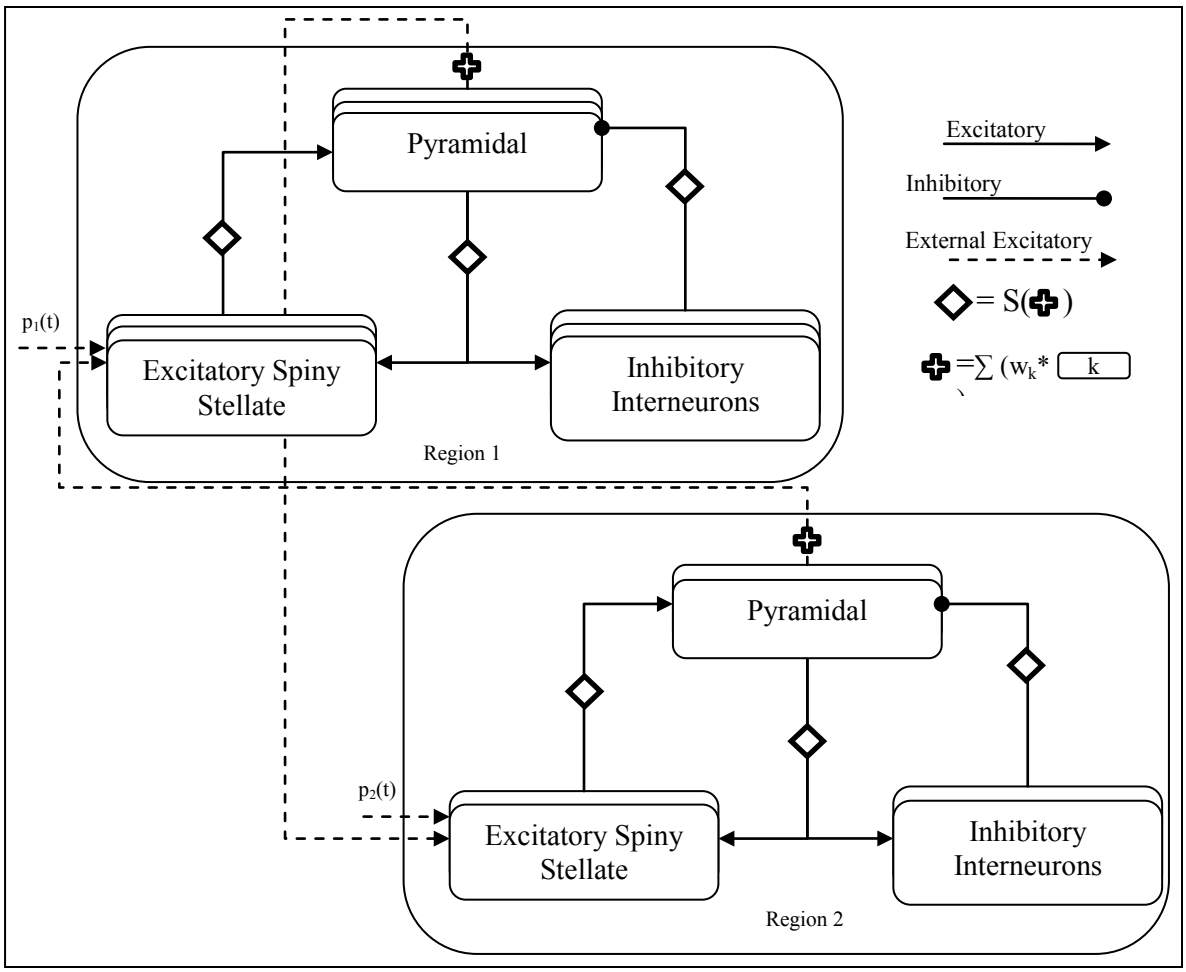

Figure 10. Architecture of two interconnected neural mass regions. Each region is composed from three columnar layers. The excitatory spiny stellate layer receives the external input coming from other regions. The pyramidal layer sends output to other regions. The interaction between the excitatory spiny stellate and inhibitory interneuron layers give rise to oscillatory activation patterns in the pyramidal layer. Each region may have multiple subpopulations, each of which drives oscillations at a different fundamental frequency. In this figure, region 1 has three internal subpopulations and region 2 has two. ✚ is the weighted sum of the sub-populations and S is the sigmoid function.

4.3.3.1 Neural Mass Region State Space

Formally, the NMM el is a dynamical system composed of six coupled first-order differential equations per subpopulation in each region. These equations were solved numerically using the fourth-order Runge-Kutta method from the SPM8 (Wellcome Department of Cognitive Neurology, University College London, London, UK) toolbox for Matlab (2011a, The Mathworks. Natick, MA.).

The equations for the state space are

Excitatory Spiny Stellate

$$\dot{v}_{u,sp,1} = x_{u,sp,1} \tag{2}$$

$$\dot{x}_{u,sp,1} = \frac{He}{\tau e} * (Network_u + External_u + .8c_0 * S(c_0 * \sum_{k=1}^{N} w_{u,k} * v_{u,k,3})) - \frac{2}{\tau e} x_{u,sp,1} - \frac{1}{\tau e^2} v_{u,sp,1} \quad (3)$$

$$Network_u = \overline{p}_u + (1 - k_{w,u}) * \tilde{p}_u(t) \quad (4)$$

$$External_u = k^*_{w,u} * \tilde{S}(y_w(t - \delta)) \quad (5)$$

$$k^*_{w,u} = \frac{\sigma_{p,u}\sqrt{2k_{w,u} - k^2_{w,u}}}{\sigma_{S(y_w)}} \quad (6)$$

where u is a neural mass region, sp is a subpopulation in region u, N is the number of subpopulations in region u, H_e tunes the maximum excitatory post synaptic potential, τ_e models properties of the dendritic tree, $Network_u$ is the input to region u from other regions in the functional network, $External_u$ is the input from sub-cortical areas, c_0 is the average number of synaptic contacts , and S is a sigmoid function that transform average membrane potential into an average rate of action potentials fired by the neurons in the region. S takes the form $S(inp) = \frac{2e_0}{1+e^{r(v_0 - inp)}}$, where e_0=2.5, r = .56, v_0 = 6. $w_{u,k}$ is the input weighting for subpopulation k, $\overline{p}_u$ is the average input from subcortical units, and $\tilde{p}_u(t)$ is the deviations from the distribution N($\overline{p}_u$,22). $k_{w,u}$ is the coupling weight for input from region w to region u. $\tilde{S}(y_w(t-\delta))$ is the standard deviation of the pyramidal output from region w at time $t - \delta$. For these simulations, δ = 10 ms and all standard deviations were computed between [t-500, $t - \delta$]. $k^*_{w,u}$ is a coupling parameter that is recomputed at each time step to ensure that the variance of the combined input from Internal and External is conserved.

Inhibitory Inter-neurons

$$\dot{v}_{u,sp,2} = x_{u,sp,2} \quad (7)$$

$$\dot{x}_{u,sp,2} = \frac{Hi}{\tau_i} * .25c_0 * S(.25c_0 * \sum_{k=1}^{N} w_{u,k} * v_{u,k,3}) - \frac{2}{\tau_i} x_{u,sp,2} - \frac{1}{\tau_i^2} v_{u,sp,2} \quad (8)$$

H_i tunes the maximum inhibitory post synaptic potential, τ_i models properties of the dendritic tree; all other parameters represent the same properties already described.

Pyramidal Cells

$$\dot{v}_{u,sp,3} = x_{u,sp,3} \quad (9)$$

$$\dot{x}_{u,sp,3} = \frac{He}{\tau_e} S(\sum_{k=1}^{N} w_{u,k} * (v_{u,k,1} - v_{u,k,2})) - \frac{2}{\tau_e} x_{u,sp,3} - \frac{1}{\tau_e^2} v_{u,sp,3} \quad (10)$$

Average Firing Rate for Region

$$y_u = \sum_{k=1}^{N} w_{u,k} * (v_{u,k,1} - v_{u,k,2}) \tag{11}$$

4.3.2 Simulation Structure

The networks were constructed by coupling two neural mass regions together. Each region of the pair was instantiated with an 11- and 43-Hz internal subpopulation. The weighting of the subpopulations was either (1) 80% of the 11-Hz subpopulation and 20% of 43-Hz subpopulation, which yielded a broadly tuned oscillator with a peak in the power spectrum at 10 Hz, or (2) 20% of the 11-Hz subpopulation and 80% of the 43-Hz subpopulation, which yielded a broadly tuned oscillator with a peak in the power spectrum at 40 Hz. All possible combinations of 10- and 40-Hz units were connected using unidirectional and bidirectional couplings for a total of seven pair combinations. Figure 11 depicts all simulated pair combinations that were instantiated.

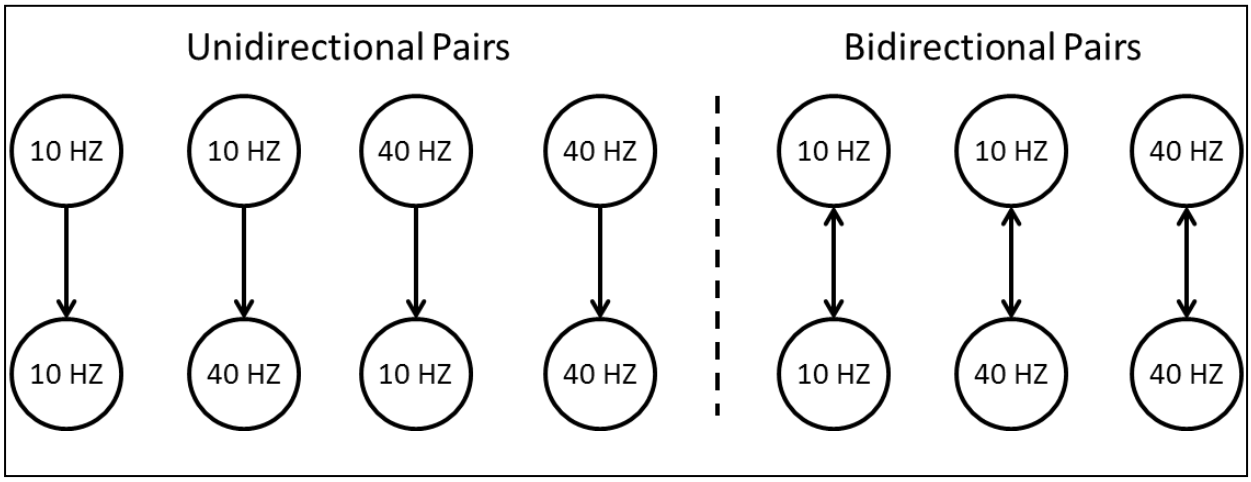

Figure 11. The seven possible combinations of 10- and 40-Hz peaked oscillator pairs over two connection types.

Ten simulated trials were performed for each pair combination. Each trial lasted for a total duration of 11 s with a sample rate of 1 ms. The first second was included to allow state-space stabilization, and it was discarded prior to computing the power spectrum and functional connectivity measures. The connection between the units was active between 1 s through 3 s and 5 s through 8 s. The connection was inactive at all other times.

4.3.3 Functional Connectivity Measures

Each of the functional connectivity measures were computed as shown in the following equations:

$$IMC = \frac{E\{Z_1 Z_2^*\}}{\sqrt{E\{|Z_1^2|\}E\{|Z_2^2|\}}} \tag{12}$$

$$PLV = | E\{e^{i(\theta_1 - \theta_2)}\} | \tag{13}$$

$$dWPLI = \frac{| E\{\Im\{Z_1 Z_2^*\}\} |}{E\{| \Im\{Z_1 Z_2^*\} |\}} \tag{14}$$

where Z_1 and Z_2 are the Fourier spectra of the two signals being compared, (*) denotes complex conjugate, and θ_1 and θ_2 are the relative phases for each signal determined by representing Z as the phasor $Z = Ae^{i\theta}$. It should be noted that the expectation operator $E\{.\}$ is taken over trials, thus the results shown were obtained by averaging over ten separate trials for each simulated condition.

To compute the functional connectivity measures over time, a moving time window of 500 ms was used with an incremental step of 25 ms. This window size was chosen empirically to provide optimal tradeoff between time and frequency resolution. Within each time window, Fourier spectra Z_1 and Z_2 were computed using the Matlab's fast Fourier transform method resulting in 2000 equally sized frequency bands spanning a frequency range of 0 to 1000 Hz. The value 2000 was determined by setting the nonequispaced fast Fourier transform (NFFT) parameter in Matlab to be four times the sample rate (1000 Hz), which meant the original signal had to be zero-padded to accurately compute the desired number of frequency components. For presentation purposes, the results have been limited to a range of 1 to 100 Hz as this contained all the oscillatory components of interest.

4.4 Results and Discussion

4.4.1 Result 1: Validation of the Neural Mass Models

The first set of results seeks to establish that the NMMs produce oscillatory firing patterns appropriate for use with phase-based functional connectivity measures. In order to establish this, two properties of the generated signals were investigated. The signal time course was examined for oscillatory patterns sensitive to whether the coupling between regions was on or off. When the coupling is on, the amplitude of the receiving region should show a large increase over when the coupling is off. This basic result should be present because the receiving region receives a larger input when the coupling is on and this increase should be reflected in the output.

The other expected property is a difference in the frequency power spectrum distribution (PSD) when the coupling is on and off. The exact nature of the change depends on the properties of the two regions and the type of connection that couples them. A unidirectional coupling should show a change in the PSD of the receiving region and an unchanged PSD in the sending region. When the coupling is in both directions, both regions should show a change in the PSD.

This section presents results from four of the seven coupled pairs that were simulated. The first two coupled pairs are identical regions coupled in both directions: one pair is a 10-Hz region coupled to another 10-Hz region, and the other pair is a 40-Hz region coupled to another 40-Hz

region. The time course activity plotted in figure 12 shows that both regions oscillate with an average depolarization between 7.4 and 7.6 when the coupling is off. When the coupling is turned on between 1 s through 3 s and 5s through 8s, they both show increases in the average depolarization. The 10 Hz ←→ 10 Hz pair oscillated with an average depolarization between 7.2 and 7.9, and the 40 Hz ←→ 40 Hz pair oscillated between 6.8 and 8.89. These changes indicate that the NMMs are sensitive to the communication between regions and show a measurable change during coupling.

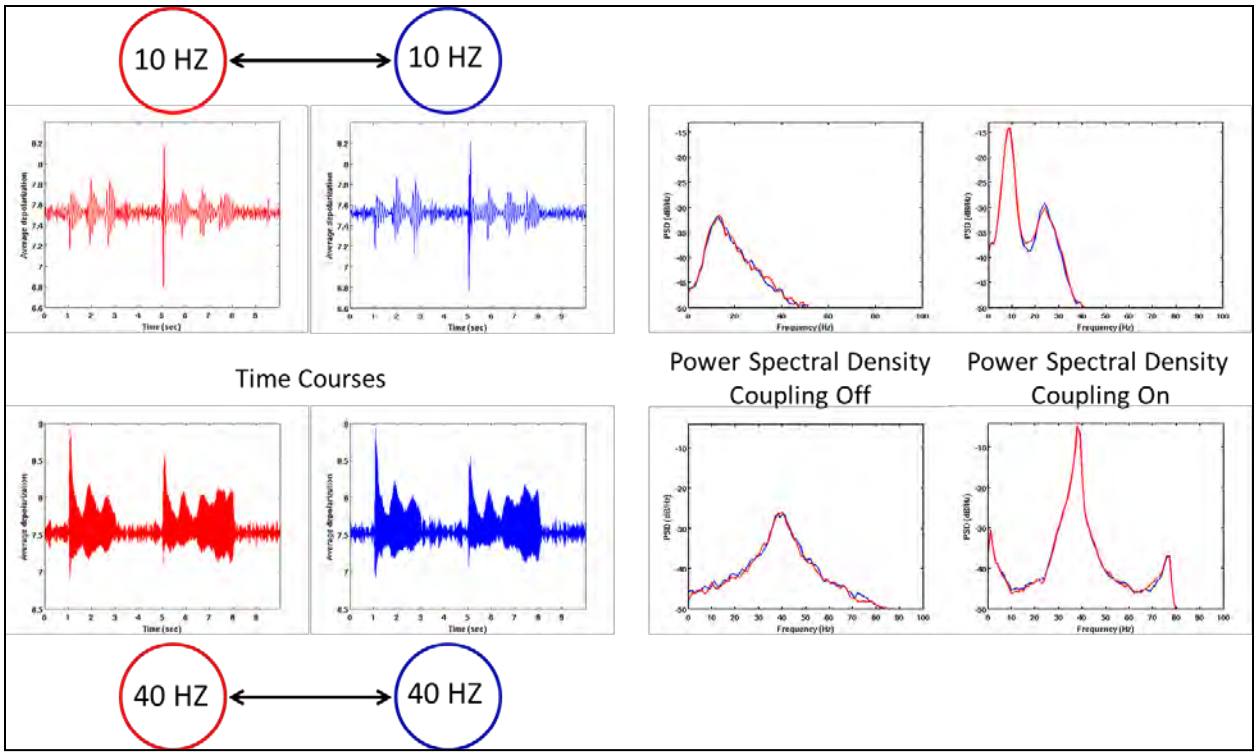

Figure 12. Time course and PSD plots for two pairs of identical bicoupled neural mass regions. Time courses show that they produce oscillatory firing patterns, and the firing rate increases greatly when the coupling is on (1–3 s and 5–8 s). Power spectral density plots show that both units have the same power distribution both when the coupling is off and on. When coupling is on, both regions show a small downshift in the peak frequency as well as a large increase in power at that frequency and its second harmonic.

Figure 12 shows that the PSD plots for both regions of a pair are virtually identical when the coupling is off; both units of the 10 Hz ←→ 10 Hz pair have identical unimodal PSDs with a peak at 10 Hz and a 1 to 50 Hz distribution. Both regions of the pair share identical bimodal PSDs when the coupling is on, but the shape of the distribution differs from the distribution when coupling is off. The central peak shifts down a small amount to 9.4 Hz when the coupling is on and has a substantial power increase compared to when the coupling is off. A second power increase is also present at a frequency close to the second harmonic of central peak.

The 40 Hz ←→ 40 Hz pair shows a similar pattern to the 10 Hz ←→ 10 Hz pair. The two regions have identical unimodal PSDs centered at 40 Hz when the coupling is off. When the

coupling is turned on, the shape of the PSD changes and this change occurs in both of the regions. Compared to the PSD when the coupling is off, the new PSD shows a small downshift in the peak frequency as well as a substantial increase in spectral power at that frequency and its second harmonic. Both the 10 Hz ←→ 10 Hz and 40 Hz ←→ 40 Hz pairs also show a large broadband spectral power increase with a 1-Hz peak. The reason for this low frequency power increase is still under investigation, but it may be due to induced synchronizations that can be seen in the amplitudes during coupling.

The second two coupled pairs are a 40-Hz region coupled in only one direction to another 40-Hz region, and 10- and 40-Hz regions coupled to each other in both directions. When the coupling is off, the time series and PSD of the 40- and 10-Hz regions are the same as those in figure 12. When the coupling is on, the sending 40-Hz region in the 40 Hz→40 Hz pair (red lines in the top row of figure 13) does not show any difference from when the coupling is off in either its time series or in the PSD plots. Conversely, the receiving region (blue lines in the top row of figure 13) shows a similar pattern to the 40-Hz units in the 40 Hz ←→ 40 Hz pair. There are significant amplitude increases in the time series and a slight down shift and large power increase of the peak frequency, its second harmonic, and at 1 Hz. Neither the amplitudes nor the powers are as strong as they were in the bidirectionally coupled variant. There are no changes between this region and two regions in 40 Hz ←→ 40 Hz pair at the timeframes when the coupling is off; this is expected since this region is not receiving any input.

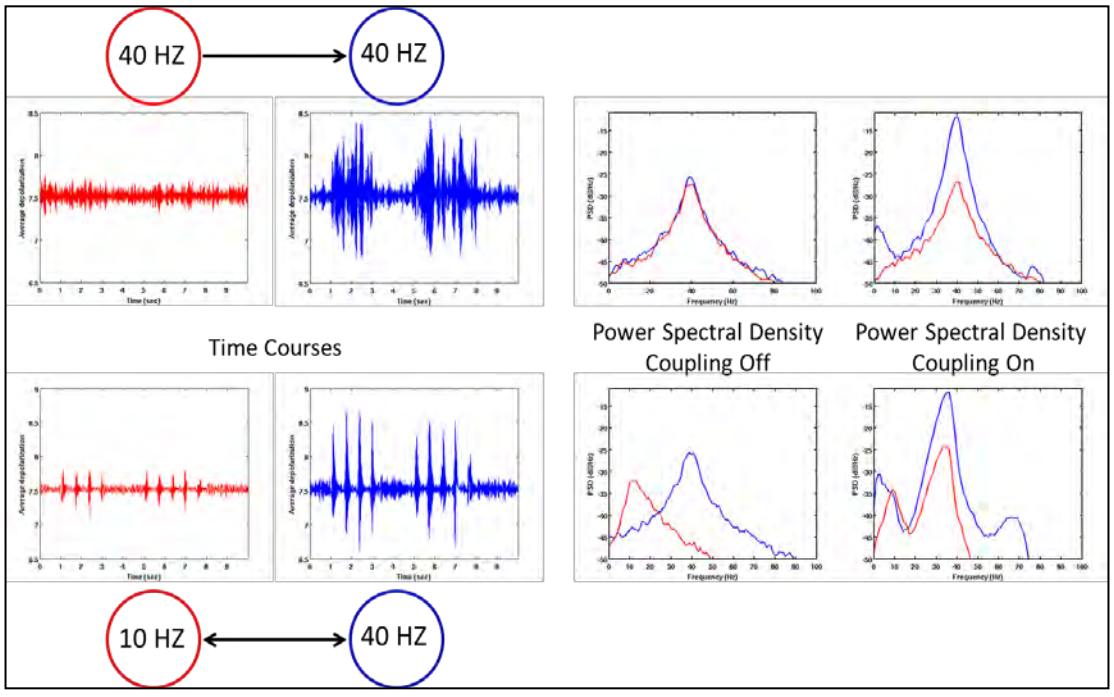

Figure 13. Time course and power spectral density plots for two pairs of NMMs. Time courses show that they produce oscillatory firing patterns and the firing rate increases greatly when the coupling is on (1–3 s and 5–8 s). Power spectral density plots show that the power distribution is different when coupling is off compared to when it is on.

When the coupling is on, the 10 Hz ←→ 40 Hz pair produces the now expected pattern of results. Both units oscillated with the same PSD observed in the other network variants when the coupling was off and had bimodal PSDs with peaks at 1 Hz, the expected frequency, and its second harmonic when coupling was on (figure 13, bottom row). The other expected result, which can be seen clearly in figure 14, is that both regions show a slight downward shift in the frequencies. The 10-Hz region's PSD peak shifted from 10 to 8 Hz and the 40-Hz region's PSD peak shifted from 40 to 35 Hz. The reason for the shift is still under investigation, but this result suggests that a pair of coupled regions can cause each other to oscillate at different frequencies than they would in isolation. Results of this type provide a potentially valuable insight for results obtained in EEG recordings. A neural region might intrinsically oscillate at a different frequency than is observed when it is processing as part of a functional network. It is also possible that the frequency at which a given region oscillates changes as a function of its functional network. This result supports such a possibility because it provides preliminary evidence that the topography of the functional network exerts an influence on a region's oscillation frequencies. Future work is necessary to examine the extent to which this manifests itself in larger networks as well as whether specific network motifs affect the likelihood of a frequency shift.

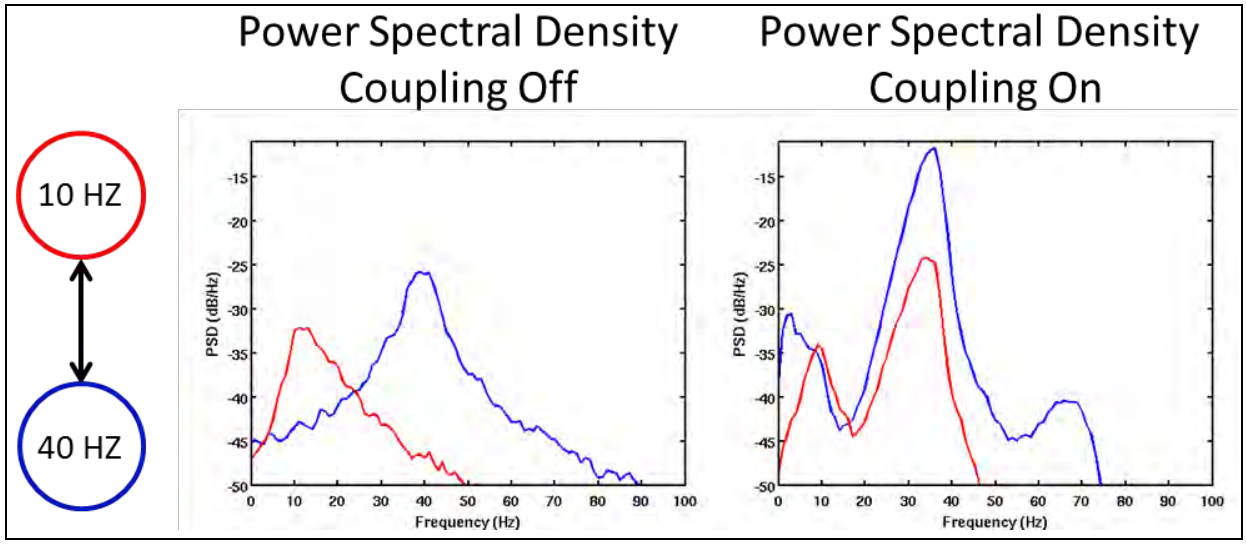

Figure 14. Power-frequency plots for 10 Hz ←→ 40 Hz pair when coupling is off and on. When the coupling is off, both units have a unimodal power distribution centered at their respective dominant frequencies. When coupling is on both units have a bimodal power distribution. One peak comes from the unit's intrinsic oscillation rate and the other arises because influences from the other unit. The most interesting part is that the coupling causes a frequency downshift in both units. The 10-Hz unit has peaks at 8 and 35 Hz and the 40-Hz unit has power peaks at 3, 7, 35, and 66 Hz.

A new, but predicted, result when coupling is on is that the PSDs of both regions contain a combination of each region's intrinsic frequency as well as an additional component coming from the other region. For example, the 10-Hz unit's PSD shows a large spectral power component at ~10 Hz and a second large component at ~35 Hz. This new component, which is not present when the coupling is off, reflects input from the 40-Hz unit. The same is true of the

PSD of the 40-Hz unit. In addition to its intrinsic frequency, it also contains an 8-Hz component coming from the 10-Hz unit when the coupling is on between the pair. Both of these results contain the expected power spectrum components from communication between regions with different intrinsic frequencies.

Collectively, these results confirm that the NMM simulation produces activations that are affected by the oscillation frequencies and connectivity of two region networks. The simulated data thus provides an avenue to validate functional connectivity measures and examine if the measures recover the time course of paired communication within the network. The simulated functional activity from each of these networks was analyzed with three undirected, phase-based functional connectivity measures (ImC, dWPLI, and PLV). Two interesting results from the measure comparison are discussed in section 4.4.2.

4.4.2 Result 2: Limitation of ImC and dWPLI

One situation in which PLV provides a better estimate of functional connectivity than ImC or dWPLI is when two identically parameterized regions are bidirectionally coupled. With this configuration, neither ImC nor dWPLI will identify the phase synchronizations induced by the functional connectivity. Figure 15 demonstrates that PLV is high when the coupling is on, whereas ImC and dWPLI return consistently low connectivity values regardless of whether coupling is on or off.

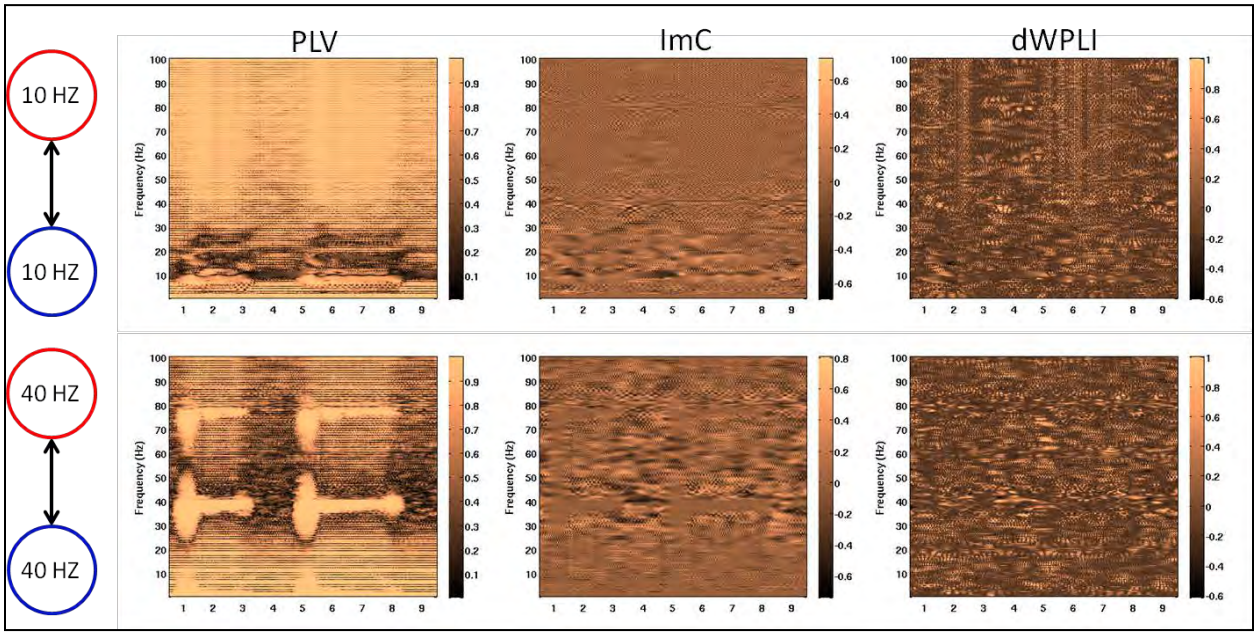

Figure 15. Phase-based functional connectivity estimates using PLV, ImC and dWPLI. Only PLV is able to identify 30–50 Hz phase synchronization but the measure also has a strong tendency to incorrectly identify phase synchronizations at lower frequencies regardless of whether the coupling is on or off. ImC and dWPLI fail to identify phase synchronizations at any frequency.

When two identical oscillators are coupled together, they very quickly synchronize their oscillations in-phase or anti-phase. Our results indicate that this is true of the NMMs even though there is a small time delay of 10 ms between the two regions. ImC and dWPLI return low values with this configuration because they were specifically constructed to do this when two signals oscillate in-phase or anti-phase. Both were designed to be resistant to noise artifacts from volume conduction, where a zero-phase relationship is discarded as artifact; however, as figure 15 shows, they also miss legitimate in-phase synchronizations produced by interacting brain regions. Interestingly if the magnitude of the value is ignored and its stability across time is examined instead, there is a clear and consistent value throughout the entire duration of communication. PLV, which does not minimize zero-phase oscillations, does identify the in-phase synchronization that occurs when the coupling is on, but it is expected that PLV will be more adversely affected by motion and environmental artifacts when tested on empirical EEG datasets collected with real-world movements and noise.

4.4.4 Result 3: dWPLI Has Greatest Sensitivity in Low Frequency Bands

All three measures successfully identify phase synchronizations in the dominate 20–60 Hz frequency range for the 40 Hz → 40 Hz pair and the 25–40 Hz frequency range for the 10 Hz ←→ 40 Hz coupled pair presented in figure 16. dWPLI is more sensitive with phase synchronization in the lower frequency bands than PLV and ImC. The 40→40 coupled pair in figure 16 (top pair) shows that dWPLI identifies a low frequency phase synchronization when the coupling transitions from off to on and again when it transitions back off. PLV also identifies low frequency phase synchronizations, but the problem is that PLV identifies so many false synchronizations when the coupling is off that is it is difficult, if not impossible, to identify the true low frequency phase synchronizations at coupling transitions. ImC, on the other hand, is not sensitive to the lower frequency synchronization at all; this is evidenced by the fact that the value is near zero across the entire time duration. Another curiosity for this pair is that the ImC and dWPLI values for this pair are consistently zero at 40 Hz. This is because of the same reason the value is zero for bidirectionally coupled pairs; during communication these two regions are oscillating in-phase or anti-phase with each other.

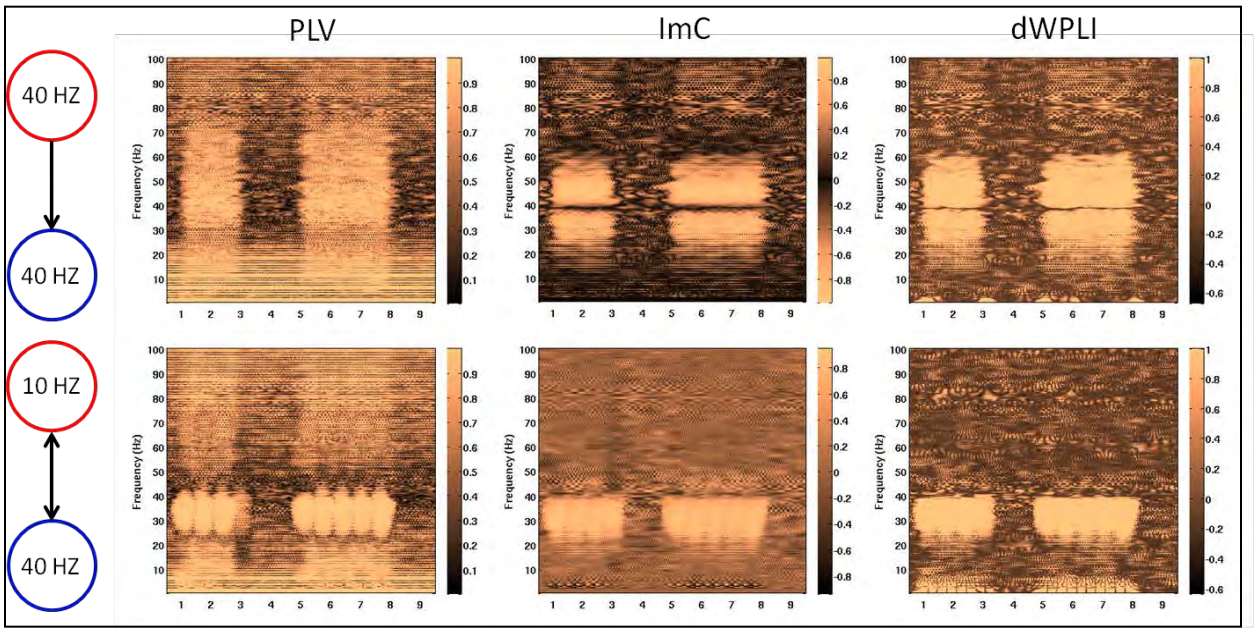

Figure 16. (D) Phase-based functional connectivity estimates using PLV, ImC and dWPLI. All three measures identify 20–60 Hz phase synchronizations when coupling is on but in the lower 1–5 Hz frequency range, only dWPLI identifies a reliable difference in phase synchronization.

The 10 Hz ←→ 40 Hz pair (figure 16, bottom) provides additional support for this claim. In this case, dWPLI identifies sustained low frequency phase synchronizations that are not reliably identified by PLV or ImC. Once again the phase synchronizations identified by PLV cannot be trusted because it also identifies many low frequency phase synchronizations at points when the coupling is off. ImC's performance is slightly better than with the previous pair. It picks up on some phase synchronization in the 3 Hz band when the coupling is on but it is still much less sensitive than dWPLI. In summary, all three measures can capture the 30–60 Hz phase synchronizations, but only dWPLI reliably identifies 1–5 Hz phase synchronization.

4.5 Conclusions

This project implemented oscillatory NMMs in order to simulate oscillatory functional activity, and then simulated data from these models were used to validate three undirected, phase-based functional connectivity measures (ImC, dWPLI, and PLV).

The first set of results established that the NMMs produce oscillatory signals, and when coupled, their output is influenced by the input coming from paired neighbors during fixed windows of communication. That is, the NMMs successfully produced oscillatory behavior and directed communication within the network. Consequently, the model appears to be a good tool to evaluate if functional connectivity measures can capture the temporal dynamics of network communication.

The second set of results indicated that all three connectivity measures capture the temporal dynamics of network communication for higher frequencies (i.e., 30–60 Hz) when nodes in the

network oscillate at different frequencies. The measures revealed different sensitivities, however, when the network communication occurred at the same frequency or the communication occurred at lower frequencies (1–5 Hz). First, only PLV could capture communication between bicoupled nodes oscillating at the same frequency, since both ImC and dWPLI were designed to minimize contribution of zero-phase signal synchronizations. This indicates the tradeoff between resilience to volume conduction noise in the signal and sensitivity to one type of oscillatory communication between network regions. Second, dWPLI captured communication at the lower frequencies within the networks most robustly. Here, the value of the PLV measure was too noisy in the lower frequencies to distinguish between coupled and uncoupled timeframes, while ImC was rather insensitive at this lower range. Combined, these results have begun to identify the relative strengths and weaknesses of each of the measures, and it suggests that this modeling effort holds promise to investigate the sensitivities of the connectivity measures in controlled, simulated networks to better understand how to interpret results.

The second set of results also indicated that the topography of the network had a significant impact on the performance of the functional connectivity measures. In the 10 Hz ←→ 40 Hz pair, the uncoupled PSD revealed the expected peaks for the intrinsic frequencies (10 and 40 Hz, respectively), but during the time windows where the two nodes are coupled, the PSDs for the nodes changed, shifting the 10 to 8 Hz and the 40 to 35 Hz. In other words, the properties of the functional network modulated the node's intrinsic oscillation frequency, and this could have important consequences for interpretation of the measure given known associations in the literature between particular frequency ranges and cognitive constructs. The hope is that developing an understanding of how functional connectivity measures are affected by network structure in a simulation where the underlying connectivity is known will provide guidance and insight for selecting which measures to use on real human data when the functional and structural networks are unknown.

Critically, future efforts will expand the model to simulate larger networks with more diverse topologies and topographies in order to better link the simulation work with empirical research. The functional networks that have been explored thus far are two unit networks with unidirectional or bidirectional connections between them. The functional networks observed in human and primate experiments have revealed functional networks consisting of dozens of interconnected regions. Systematically examining network topology, interconnectivity, and topology has potential for helping with the interpretation of functional connectivity results obtained from more complex networks. Larger networks may provide more unforeseen insights into the effect of network configuration on functional connectivity measures. Larger networks will also allow for a more thorough and systematic examination of how different network configurations change the intrinsic oscillations of the regions.

A second important avenue for future research is a thorough exploration of the parameter space. Specifically, it is important to understand which parameters are stable with respect to variation and which parameters cause instabilities when changed. Expanding to larger networks may cause

the models to become unstable when using the current parameter values. Furthermore, growing the networks to dozens (or hundreds) of regions may require introducing strong boundary conditions over some parameters. Systematically studying the sensitivity of parameters to variation will provide insight into which parameters may require these strong boundary conditions. In addition, the stability of a parameter may be modulated by the size of the network, since some parameters that do not play a significant role in small networks may become more sensitive as the networks become larger.

In summary, the results here indicate that the NMM simulation can reproduce expected oscillatory behavior in two-node networks, and even these simple networks capture substantial differences among the three tested functional connectivity measures. Future efforts will explore larger networks, parameters to keep those larger network stable, and additional types and classes of functional connectivity measures. This simulation work is expected to augment empirical efforts to develop and validate functional connectivity measures in order to understand network-based brain dynamics in complex, Army-relevant settings.

5. Project 4: Design and Implementation of a Numerical Technique to Inform Anisotropic Hyperelastic Finite Element Models Using Diffusion-weighted Imaging

5.1 Authors

The authors on this project are Reuben H. Kraft ARL/WMRD and Amy M. Dagro ARL/WMRD (ARL-TR-5796, in press).

5.2 Introduction

Anisotropy is prevalent in numerous biological tissues, which are comprised of fibers, or bundles of cells, aligned in a uniform direction. For example, within the white matter regions of the human brain, axons tend to form complex fiber tracts that promote anatomical connectivity and communication. The bundles of axonal fibers can be visualized using noninvasive tools such as diffusion tensor magnetic resonance medical imaging (DTI). The basic principle behind DTI is that water diffuses more rapidly in the direction aligned with the internal structure and more slowly as it moves perpendicular to the preferred direction. From the diffusion tensor computed from the imaging, diffusion anisotropy measures such as the FA can further be computed. In addition, the principal direction of the diffusion tensor can be used to estimate the white matter connectivity of the brain. Visualization of the white matter connectivity is called tractography. An example of DTI tractography is shown in figure 17. Note that DTI is one particular method or application of the broader DWI.

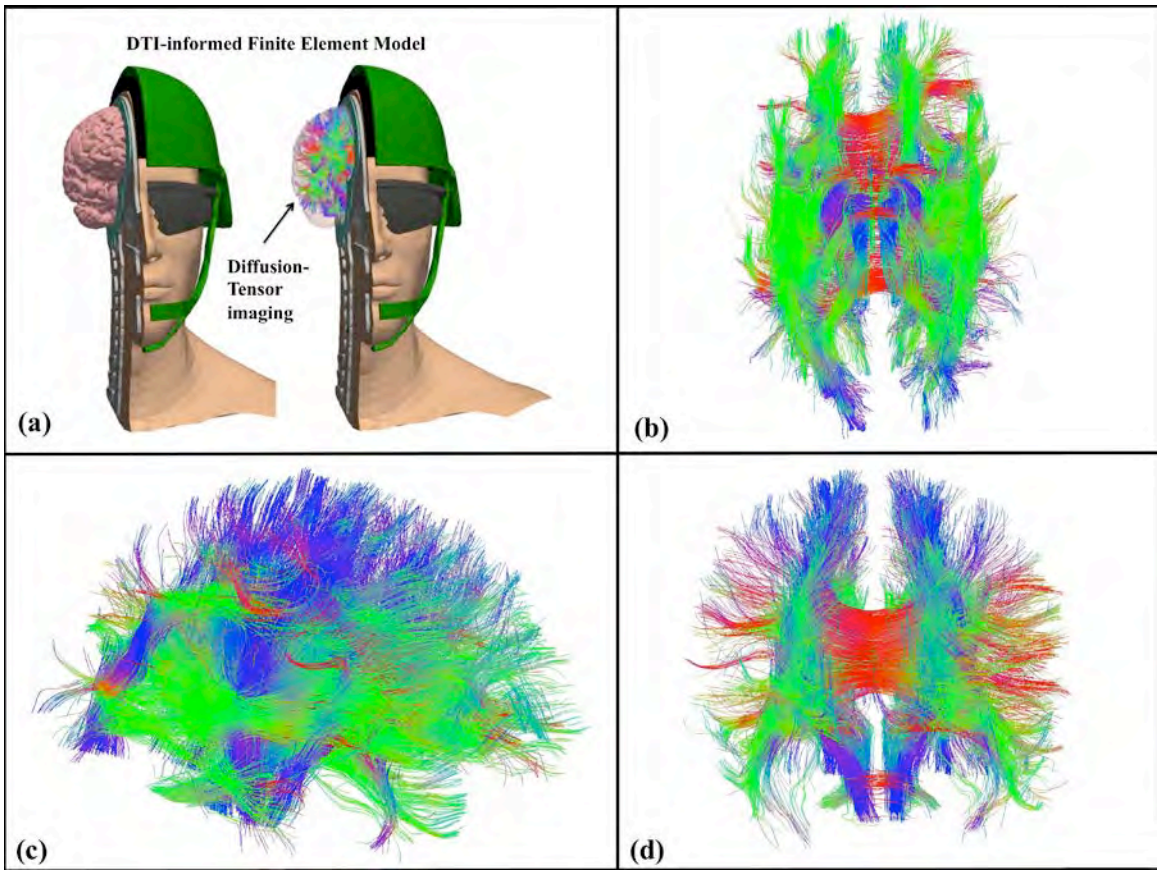

Figure 17. Using DTI, axonal fiber tractography can be overlaid on a finite element mesh and used to construct a transversely isotropic model. Tractography consists of complex fibers shown from (b) dorsal, (c) right lateral side, and (d) posterior views.

The anisotropic properties of biological tissue are important to capture within a computational framework because the axonal fiber tracts have been reported to be approximately three times stiffer than the surrounding matrix (Arbogast et al., 1999). In fact, numerous efforts have focused on incorporating details of fiber tractography into a computational framework where many use transversely isotropic viscoelastic constitutive models to represent the bulk and fiber mixture. For example, Ning et al. (2006) conduct experiments and optimization techniques to develop a transversely isotropic viscoelastic constitutive model for a porcine brain stem tissue sample. Wright et al. present an analytical and computational model that also treats the white matter as an anisotropic, hyperelastic material using DTI to incorporate the structural orientation of the neural axons into the model. Wright et al. show that the degree of injury that is predicted in a computational model of DTI is highly dependent on the incorporation of the axonal orientation information and the inclusion of anisotropy into the constitutive model for white matter.

The work presented here extends previous efforts by using the transversely isotropic hyperelastic model formulation, and describes a new design and implementation for informing the finite element model using DTI in a three-dimensional, parallel computing framework. Besides biological materials, the algorithms described in this report can be applied to a broad range of

engineering materials, as well. For example, Kevlar armor protection systems contain fiber directions that rotate with the curvature of the surface. The finite element implementation included here sets the appropriate framework for incorporating fiber directions into finite element models used in a diverse range of applications.

In this report, we begin by describing the continuum theory behind the implementation of the transversely isotropic hyperelastic model in section 5.3.1 followed by results of a validation study of the implementation within the finite element framework in section 5.3.2. Then, section 5.3.3 presents an algorithm for linking DTI and the transverse isotropic model. Section 5.3.4 discusses an extension of the research to modeling the white matter tissue of the human brain in a three-dimensional finite element code. Then section 5.3.5 offers some concluding remarks and opportunities for future work.

5.3 Methods, Results, and Discussion

5.3.1 Continuum Theory of Transversely Isotropic Hyperelasticity

5.3.1.1 Kinematics of Finite Deformations

We begin by defining the deformation gradient defined as

$$\overline{\mathbf{F}} = J^{-1/3}\mathbf{F} \tag{15}$$

where **x** is the deformed configuration of a material particle and **X** is the reference position. The ratio of deformed to undeformed volumes is given by the determinant of **F**:

$$J = \det(\mathbf{F}) \tag{16}$$

Some materials behave differently in bulk and shear, so it is most beneficial to perform a multiplicative decomposition of **F** into volume-changing (dilational) and volume-preserving (distortional) parts (equation 18). To do this, a deviatoric deformation gradient is defined in which the volume change is eliminated:

$$\overline{\mathbf{F}} = J^{-1/3}\mathbf{F} \tag{17}$$

It then follows that:

$$\overline{\mathbf{C}} = \overline{\mathbf{F}}^T\overline{\mathbf{F}} \tag{18}$$

$$\overline{\mathbf{B}} = \overline{\mathbf{F}}\,\overline{\mathbf{F}}^T \tag{19}$$

where $\overline{\mathbf{C}}$ and $\overline{\mathbf{B}}$ are referred to as the modified right Cauchy-Green tensor, and the modified left Cauchy-Green tensor, respectively. The modified principle invariants of the Cauchy-Green deformation tensor are

$$\bar{I}_1 = \operatorname{tr}\bar{\mathbf{C}} = \operatorname{tr}\bar{\mathbf{B}} \tag{20}$$

$$\bar{I}_2 = \frac{1}{2}\left[\left(\operatorname{tr}\bar{\mathbf{C}}\right)^2 - \operatorname{tr}\left(\bar{\mathbf{C}}^2\right)\right] = \frac{1}{2}\left[\left(\operatorname{tr}\bar{\mathbf{B}}\right)^2 - \operatorname{tr}\left(\bar{\mathbf{B}}^2\right)\right] \tag{21}$$

$$\bar{I}_3 = \det\bar{\mathbf{C}} = \det\bar{\mathbf{B}} \tag{22}$$

Two additional invariants are introduced in order to capture the mechanics of transverse isotropic materials:

$$\bar{I}_4 = \mathbf{a}_0 \cdot \bar{\mathbf{C}}\mathbf{a}_0 \tag{23}$$

$$\bar{I}_5 = \mathbf{a}_0 \cdot \bar{\mathbf{C}}^2\mathbf{a}_0 \tag{24}$$

where $\bar{I}_4$ and $\bar{I}_5$ arise directly from the anisotropy and describe the properties of the fiber family and its interaction with the other material constituents. The vector $\mathbf{a}_0$ is introduced to describe the undeformed fiber direction where we have assumed that the only anisotropic property of the solid comes from the presence of the fibers. For a material that is reinforced by only one family of fibers, the stress at a material point depends not only on the deformation gradient **F**, but also on that single preferred direction, which is called the fiber direction.

5.3.1.2 Decoupled Representation of Strain Energy

Following the approach taken by others (Ning et al., 2006; Holzapfel et al., 2000; Weiss et al., 1996) in the representation of transversely isotropic hyperelasticity, a unique decoupled representation of the strain energy function per unit volume in terms of the five invariants is given by

$$\Psi(\bar{I}_1, \bar{I}_2, \bar{I}_3, \bar{I}_4, \bar{I}_5) = \Psi_{\text{iso}}(\bar{I}_1, \bar{I}_2, \bar{I}_3) + \Psi_{\text{aniso}}(\bar{I}_4, \bar{I}_5) \tag{25}$$

where $\Psi_{\text{iso}}(\bar{I}_1, \bar{I}_2, \bar{I}_3)$ describes the response of the isotropic matrix, and $\Psi_{\text{aniso}}(\bar{I}_4, \bar{I}_5)$ describes the directional contribution of the fiber reinforcement. Note that for an incompressible material, $\bar{I}_3 = J^2 = 1$.

5.3.1.3 Uncoupled Stress Tensor

For a hyperelastic material, the 2nd Piola-Kirchhoff stress is derived from the strain energy as

$$\mathbf{S} = 2\frac{\partial\Psi}{\partial\mathbf{C}} \tag{26}$$

$$= 2J^{-2/3}\operatorname{DEV}\left[\frac{\partial\bar{\Psi}\left(\bar{\mathbf{C}}\right)}{\partial\bar{\mathbf{C}}}\right] - pJ\mathbf{C}^{-1} \tag{27}$$

where the operator $\operatorname{DEV}[\cdot] = [\cdot] - \frac{1}{3}\left([\cdot] : \bar{\mathbf{C}}\right)\bar{\mathbf{C}}^{-1}$ extracts the deviatoric part of a tensor in the reference configuration and $p = -\frac{\partial\Psi}{\partial J}$ is the hydrostatic pressure. Using the chain rule, equation 27 can be further written as

$$\mathbf{S} = 2J^{-2/3}\mathrm{DEV}\left[\sum_{a=1-5,a\neq 3}\left(\frac{\partial\Psi}{\partial\overline{I}_a}\frac{\partial\overline{I}_a}{\partial\overline{\mathbf{C}}}\right)\right] - pJ\mathbf{C}^{-1} \tag{28}$$

where the terms $\frac{\partial I_a}{\partial \overline{\mathbf{C}}}$ are given as:

$$\frac{\partial\overline{I}_1}{\partial\overline{\mathbf{C}}} = \mathbf{I} \tag{29}$$

$$\frac{\partial\overline{I}_2}{\partial\overline{\mathbf{C}}} = \overline{I}_1\mathbf{I} - \overline{\mathbf{C}} \tag{30}$$

$$\frac{\partial\overline{I}_4}{\partial\overline{\mathbf{C}}} = \mathbf{a}_0 \otimes \mathbf{a}_0 \tag{31}$$

$$\frac{\partial\overline{I}_5}{\partial\overline{\mathbf{C}}} = \mathbf{a}_0 \otimes \overline{\mathbf{C}}\cdot\mathbf{a}_0 + \mathbf{a}_0 \cdot \overline{\mathbf{C}} \otimes \mathbf{a}_0 \tag{32}$$

where **I** is a 2nd rank identity tensor.

A push-forward operation on the second Piola-Kirchoff stress tensor **S** to the current configuration, and a scaling with the inverse of the volume ratio, transforms equation 30 to the Cauchy stress tensor of a transversely isotropic, compressible hyperelastic material:

$$\sigma = \frac{2}{J}\mathrm{dev}\left[\overline{\mathbf{F}}\frac{\partial\Psi}{\partial\overline{\mathbf{C}}}\overline{\mathbf{F}}^T\right] - p\mathbf{I} \tag{33}$$

$$\sigma = \frac{2}{J}\mathrm{dev}\left[\left(\Psi_1 + \overline{I}_1\Psi_2\right)\overline{\mathbf{B}} - \Psi_2\overline{\mathbf{B}}^2 + \overline{I}_4\Psi_4\mathbf{a}\otimes\mathbf{a} + \overline{I}_4\Psi_5\left(\mathbf{a}\otimes\overline{\mathbf{B}}\mathbf{a} + \mathbf{a}\overline{\mathbf{B}}\otimes\mathbf{a}\right)\right] - p\mathbf{I} \tag{34}$$

where

$$\mathrm{dev}\left[\cdot\right] = \left[\cdot\right] - \frac{1}{3}\left(\left[\cdot\right] : \mathbf{I}\right)\mathbf{I} \tag{35}$$

$$\Psi_i = \frac{\partial\Psi}{\partial\overline{I}_i} \tag{36}$$

$$\mathbf{a} = \mathbf{F}\mathbf{a}_0 \tag{37}$$

in which a describes the configuration of a_0 during the deformation.

5.3.1.3 Uncoupled Stress Tensor for a Particular Ψ

Within the framework of incompressible, transversely isotropic hyperelasticity, the strain energy function can be written in the uncoupled form as

$$\Psi(\mathbf{C}) = \Psi_{\mathrm{vol}}(J) + \overline{\Psi_{\mathrm{isoc}}}(\overline{\mathbf{C}}) \tag{38}$$

where $\Psi_{vol}(J)$ represents the volumetric strain energy contribution and $\overline{\Psi_{isoc}}(\overline{\mathbf{C}})$ represents the isochoric strain energy function. Following Weiss et al. (1996), the isochoric part of the strain energy can be further subdivided into separate functions associated with the modified invariants:

$$\Psi(\mathbf{C}) = \Psi_{vol}(J) + \overline{F}_1\left(\overline{I}_1, \overline{I}_2\right) + \overline{F}_2\left(\overline{I}_4\right) \tag{39}$$

with:

$$\overline{F}_1 = C_1\left(\overline{I}_1 - 3\right) + C_2\left(\overline{I}_2 - 3\right) \tag{40}$$

$$\overline{F}_2 = C_3\left[\exp\left(\overline{I}_4 - 1\right) - \overline{I}_4\right] \tag{41}$$

where C_1, C_2, and C_3 are constants obtained from parameter fits to experimental data. Equation 40 corresponds to a modified Mooney-Rivlin model, and equation 27 describes an exponential behavior in the fiber direction that is a characteristic of most soft tissues.

Then, similar to equation 27, the second Piola-Kirchoff stress is given by

$$\mathbf{S} = 2J^{-2/3}\mathrm{DEV}\left[\frac{\partial\overline{\Psi_{isoc}}\left(\overline{\mathbf{C}}\right)}{\partial\overline{\mathbf{C}}}\right] - \frac{\partial\Psi_{vol}\left(J\right)}{\partial J}J\mathbf{C}^{-1} \tag{42}$$

where the partial derivative of the isochoric part is given by

$$\frac{\partial\overline{\Psi_{isoc}}\left(\overline{\mathbf{C}}\right)}{\partial\overline{\mathbf{C}}} = \left[\frac{\partial\overline{\Psi_{isoc}}\left(\overline{\mathbf{C}}\right)}{\partial\overline{I}_1} + \frac{\partial\overline{\Psi_{isoc}}\left(\overline{\mathbf{C}}\right)}{\partial\overline{I}_2}\overline{I}_1\right]\mathbf{I} - \frac{\partial\overline{\Psi_{isoc}}\left(\overline{\mathbf{C}}\right)}{\partial\overline{I}_2}\overline{\mathbf{C}} + \frac{\partial\overline{\Psi_{isoc}}\left(\overline{\mathbf{C}}\right)}{\partial\overline{I}_4}\mathbf{a}_0\otimes\mathbf{a}_0 \tag{43}$$

so then substituting equation 43 into the DEV operator in equation 42

$$\begin{aligned}\mathrm{DEV}\left[\frac{\partial\overline{\Psi_{isoc}}\left(\overline{\mathbf{C}}\right)}{\partial\overline{\mathbf{C}}}\right] &= \left[\frac{\partial\overline{\Psi_{isoc}}\left(\overline{\mathbf{C}}\right)}{\partial\overline{I}_1} + \frac{\partial\overline{\Psi_{isoc}}\left(\overline{\mathbf{C}}\right)}{\partial\overline{I}_2}\overline{I}_1\right]\mathbf{I} - \frac{\partial\overline{\Psi_{isoc}}\left(\overline{\mathbf{C}}\right)}{\partial\overline{I}_2}\overline{\mathbf{C}} + \frac{\partial\overline{\Psi_{isoc}}\left(\overline{\mathbf{C}}\right)}{\partial\overline{I}_4}\mathbf{a}_0\otimes\mathbf{a}_0 \\ &- \frac{1}{3}\left[\frac{\partial\overline{\Psi_{isoc}}\left(\overline{\mathbf{C}}\right)}{\partial\overline{I}_1}\overline{I}_1 + 2\frac{\partial\overline{\Psi_{isoc}}\left(\overline{\mathbf{C}}\right)}{\partial\overline{I}_2}\overline{I}_2 + \frac{\partial\overline{\Psi_{isoc}}\left(\overline{\mathbf{C}}\right)}{\partial\overline{I}_4}\overline{I}_4\right]\mathbf{C}^{-1}\end{aligned} \tag{44}$$

Then, the second Piola-Kirchoff stress is given by

$$\begin{aligned}\mathbf{S} = 2J^{-2/3}\Bigg[&\left(\frac{\partial\overline{\Psi_{isoc}}\left(\overline{\mathbf{C}}\right)}{\partial\overline{I}_1} + \frac{\partial\overline{\Psi_{isoc}}\left(\overline{\mathbf{C}}\right)}{\partial\overline{I}_2}\overline{I}_1\right)\mathbf{I} - \frac{\partial\overline{\Psi_{isoc}}\left(\overline{\mathbf{C}}\right)}{\partial\overline{I}_2}\overline{\mathbf{C}} + \frac{\partial\overline{\Psi_{isoc}}\left(\overline{\mathbf{C}}\right)}{\partial\overline{I}_4}\mathbf{a}_0\otimes\mathbf{a}_0 \\ &-\frac{1}{3}\left(\frac{\partial\overline{\Psi_{isoc}}\left(\overline{\mathbf{C}}\right)}{\partial\overline{I}_1}\overline{I}_1 + 2\frac{\partial\overline{\Psi_{isoc}}\left(\overline{\mathbf{C}}\right)}{\partial\overline{I}_2}\overline{I}_2 + \frac{\partial\overline{\Psi_{isoc}}\left(\overline{\mathbf{C}}\right)}{\partial\overline{I}_4}\overline{I}_4\right)\mathbf{C}^{-1}\Bigg] - \frac{\partial\Psi_{vol}\left(J\right)}{\partial J}J\mathbf{C}^{-1}\end{aligned} \tag{45}$$

where

$$\frac{\partial \Psi_{\text{vol}}(J)}{\partial J} = p \tag{46}$$

$$\frac{\partial \overline{\Psi}_{\text{isoc}}(\overline{\mathbf{C}})}{\partial \overline{I}_1} = C_1 \tag{47}$$

$$\frac{\partial \overline{\Psi}_{\text{isoc}}(\overline{\mathbf{C}})}{\partial \overline{I}_2} = C_2 \tag{48}$$

$$\frac{\partial \overline{\Psi}_{\text{isoc}}(\overline{\mathbf{C}})}{\partial \overline{I}_4} = C_3\left[\exp\left(\overline{I}_4 - 1\right) - 1\right] \tag{49}$$

Then, substituting into equation 45

$$\begin{aligned}\mathbf{S} = &-pJ\mathbf{C}^{-1} + \\ &2J^{-2/3}\left[\left(C_1 + C_2\overline{I}_1\right)\mathbf{I} - C_2\overline{\mathbf{C}} + C_3\left[\exp\left(\overline{I}_4 - 1\right) - 1\right]\mathbf{a}_0 \otimes \mathbf{a}_0\right. \\ &\left.-1/3\left(C_1\overline{I}_1 + 2C_2\overline{I}_2 + C_3\left[\exp\left(\overline{I}_4 - 1\right) - 1\right]\overline{I}_4\right)\mathbf{C}^{-1}\right]\end{aligned} \tag{50}$$

a push-forward operation yields the Cauchy stress:

$$\begin{aligned}\sigma = &-p\mathbf{I} + \\ &\frac{2}{J}\left[\left(C_1 + C_2\overline{I}_1\right)\overline{\mathbf{B}} - C_2\overline{\mathbf{B}}^2 + C_3\left[\exp\left(\overline{I}_4 - 1\right) - 1\right]\mathbf{a} \otimes \mathbf{a}\right. \\ &\left.-1/3\left(C_1\overline{I}_1 + 2C_2\overline{I}_2 + C_3\left[\exp\left(\overline{I}_4 - 1\right) - 1\right]\overline{I}_4\right)\mathbf{I}\right]\end{aligned} \tag{51}$$

5.3.2 Validation of Numerical Method

To insure that the stress update was properly implemented into the computational framework, numerical tests were performed and compared to an analytical solution. Single element computations of uniaxial, strip biaxial, and equibiaxial tests were performed to validate the update of the stress for the implementation against theoretical solutions. If the stresses are applied in the *x*-*y* plane along the principal axes so the σ_{zz} component is zero and the incompressibility constraint det **F** = 1 is applied, the deformation gradient can be expressed as

$$F = \begin{bmatrix} \lambda_x & 0 & 0 \\ 0 & \lambda_y & 0 \\ 0 & 0 & \frac{1}{\lambda_x \lambda_y} \end{bmatrix} \tag{52}$$

Then using equation 51, the stresses are

$$\sigma_{xx} = 2\left[\left(C_1 + C_2\overline{I}_1\right)\left(\overline{B}_{xx} - \overline{B}_{zz}\right) - C_2\left(\overline{B}_{xx}^2 - \overline{B}_{zz}^2\right) + C_3\left[\exp\left(\overline{I}_4 - 1\right) - 1\right]\overline{I}_4\left(a_x^2 - a_z^2\right)\right] \tag{53}$$

$$\sigma_{yy} = 2\left[\left(C_1 + C_2\overline{I}_1\right)\left(\overline{B}_{yy} - \overline{B}_{zz}\right) - C_2\left(\overline{B}_{yy}^2 - \overline{B}_{zz}^2\right) + C_3\left[\exp\left(\overline{I}_4 - 1\right) - 1\right]\overline{I}_4\left(a_y^2 - a_z^2\right)\right] \tag{54}$$

In the case of uniaxial extension, $\sigma_{yy} = \sigma_{zz} = 0$ and $\lambda_y = \lambda_z$. For a strip biaxial test, $\sigma_{zz} = 0$ and $\lambda_z = 1$. For an equibiaxial test, $\sigma_{zz} = 0$ and $\lambda_x = \lambda_y$. In addition, the same material constants were used for all three cases including, $C_1 = 10.0$, $C_2 = 10.0$, $C_3 = 100.0$, and $\kappa = 10.0e9$. As seen in figure 18, good agreement between the theoretical and finite element solutions for all three cases of loading is achieved. The convergence of the finite element solution to the theoretical solution demonstrates that the stress update equations were implemented correctly.

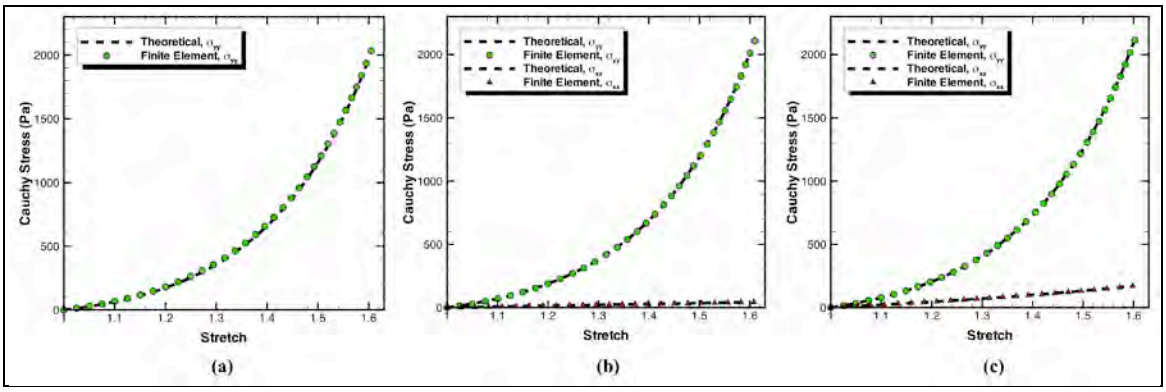

Figure 18. Comparison between the finite element results and analytic solutions for three different loading conditions: (a) uniaxial, (b) strip biaxial, and (c) equibiaxial.

5.3.3 An Algorithm for Linking DTI and Continuum Mechanics

The transversely isotropic hyperelastic model previously implemented depends on the fiber reinforcement in the undeformed configuration, $\mathbf{a}_0$. The algorithm developed here describes how to assign each finite element an orientation based on the fiber tractography obtained from DTI, as introduced in section 5.3.1. This is complex because of the nonlinear tractography and unstructured finite element shapes within the three-dimensional framework. Algorithms for both hexahedral and tetrahedral elements are described.

First, the algorithm divides each fiber line, *f*i (where i goes between 0 and the number of tractography fibers), into individual fiber segments, sj (where j goes between 1 and the number of segments within a given fiber line). Each fiber segment consists of two fiber segment points with coordinates p_1 and p_2: $s = p_2 - p_1$. The first discretized point within the fiber segment is assigned a direction based on the vector connecting it to the second point. If the fiber point exists

at the end of a fiber line, that terminating point receives the same orientation as the previous point. A schematic of the discretization process is shown in figure 19.

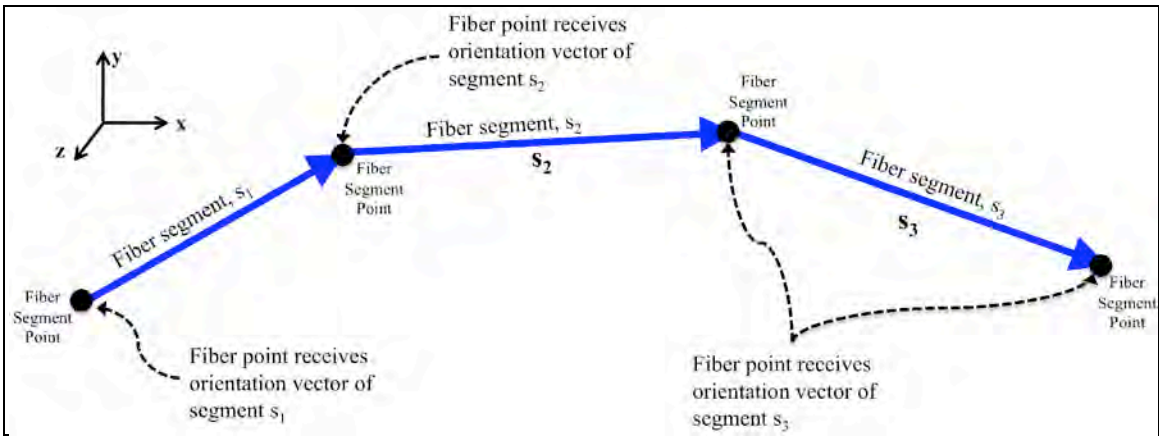

Figure 19. Fiber discretization and notation definitions used throughout the report.

Next, the algorithm determines if a fiber segment within a given tractography fiber overlaps spatially with a finite element. In order to determine this, various cases need to be analyzed. We begin our search algorithm at the fiber segment end points. For each element in the volumetric mesh, every point within each fiber is analyzed for the cases schematically shown in figure 20. Case 1 exists if the first point in a fiber segment is contained in a given element. Case 2 exists if the second point of a fiber segment is contained in a given element. Case 3 exists if both end points of the fiber segment are contained within a given element. Case 4 exists if a fiber segment intersects the faces of the element, but its fiber points are not contained within a given element. Case 5 exists if the element contains none of the fiber points and the segment does not intersect the element faces. Note, that there is an unlikely subset of case3 when a given fiber segment lies parallel with a single element face, so this orientation would be shared by any adjacent element also.

For all of the cases shown in figure 20, determining if a fiber point is contained within a finite element is complicated by the unstructured mesh shapes. For example, in elements with adjacent faces far from orthogonal with each other, a fiber point may lie outside of the faces of the element even if the fiber point spatial coordinates are in the bounds of the maximum and minimum element nodal coordinates. Therefore, an algorithm to determine if the fiber point is inside of the element is implemented. The algorithm takes into consideration the angles of the element faces explicitly by computing normals to the element faces and the coordinates of the fiber point, as schematically shown in figure 21.

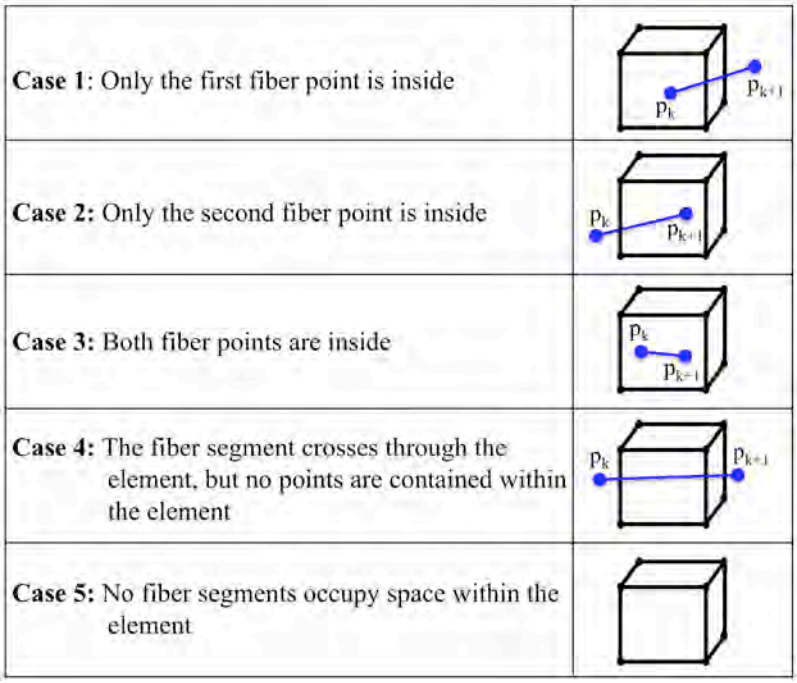

Figure 20. Schematic of the various cases that are possible when determining if a fiber segment (within a given tractography fiber) overlaps with a finite element in space.

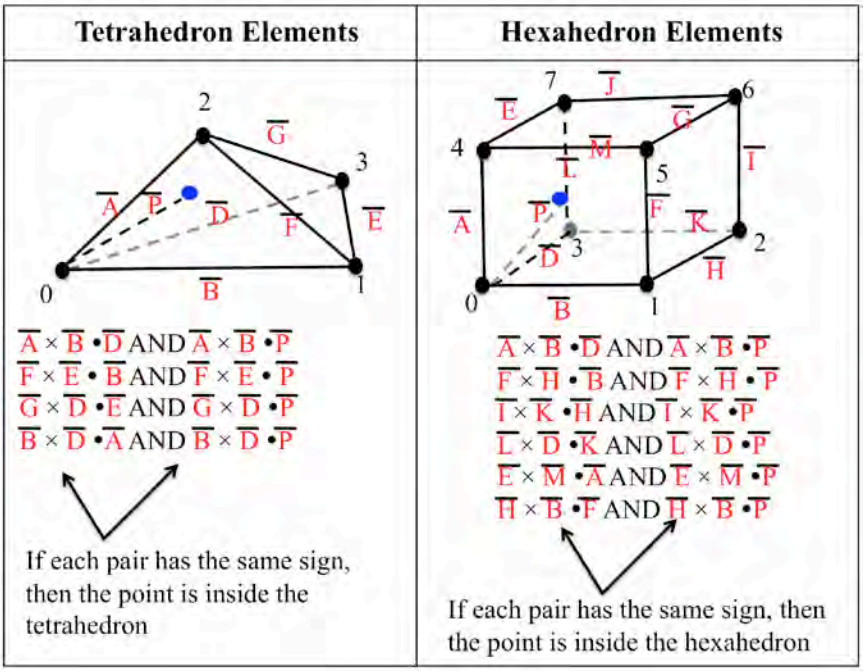

Figure 21. Method used to test if a specified point is within the element. Algorithms for both tetrahedron and hexahedron elements are designed and implemented.

A slightly more complicated algorithm is used for case 4 where the line segment intersects the element faces, but no points in the fiber segment reside within the element.

As schematically shown in figure 22, first the algorithm calculates the normal of the first face, n by taking the cross product of two vectors, which share the same vertex, P_1.

$$\mathbf{n} = (P_2 - P_1) \times (P_3 - P_1) \tag{55}$$

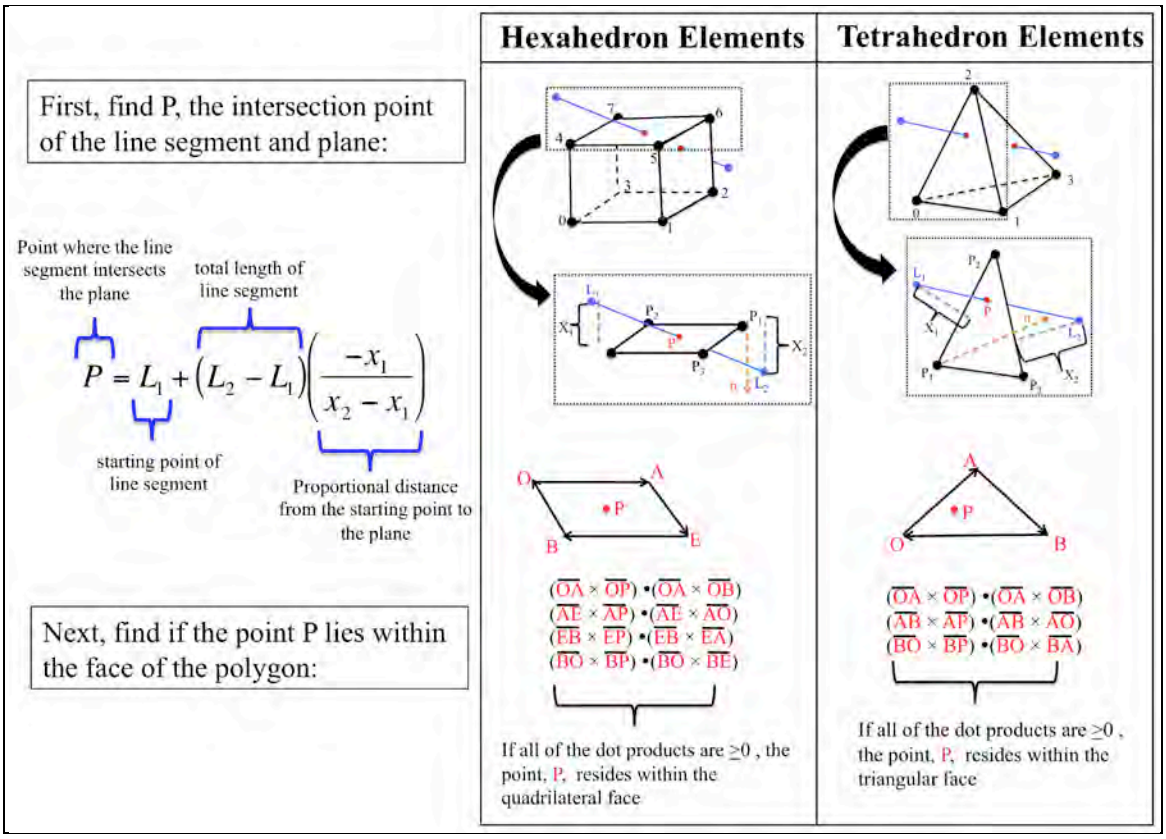

Figure 22. Method used to test if a line intersects the faces of an element for the case in which the line segment intersects the element faces, but no points in the segment reside within the element (see Case 4 in figure 20).

Next, the algorithm takes the dot product of the distance between an endpoint, L_1 or L_2, and the shared vertex P_1. This results in two dot products, the distances from L_1 and L_2 from P_1:

$$x_1 = (L_1 - P_1) \cdot (\mathbf{n}) \tag{56}$$

$$x_2 = (L_2 - P_1) \cdot (\mathbf{n}) \tag{57}$$

If $x_1\, x_2 \geq 0$, the line segment never intersects the plane of the face. If $x_1 = x_2$, the line segment and the plane are parallel, and the line segment can be disregarded since it does not intersect two different faces of the element. If the two preceding conditions do not exist, the code will find the location of the point, P, on the given line segment which intersects the plane.

$$P = L_1 + (L_2 - L_1)\left(\frac{-x_1}{x_2 - x_1}\right) \tag{58}$$

The point P is the intersection point that exists on the plane of the element face; therefore, the algorithm must test if P also lies within the surface area of an element face (see figure 22). A point is inside of a polygon if it is always on the same side of all the segments that create a continuous loop around the edges. For a given fiber segment that solely intersects the element faces, there should be exactly two intersection points on a single element.

If there exist elements for a given finite element mesh where no fiber tracks overlap, the elements are assigned an orientation vector of zero, $\mathbf{a}_0 = 0$. Therefore, the transversely isotropic material condenses to an isotropic material.

5.3.4 A Scheme for Averaging Multiple Fibers

The previous discussion described the methods used to find the existence and direction of a single fiber in a hexahedral or tetrahedral element. The fiber direction assigned to an element with only one fiber segment is given by

$$\mathbf{a}_0 = \frac{\mathbf{s}}{||\mathbf{s}||} \tag{59}$$

where **s** represents the orientation vector of the fiber segment. Depending on the fiber or mesh densities, there could be multiple fibers, multiple fiber segments, or both existing in a single element, as schematically depicted in figure 23. The current effort develops an average scheme for each possibility since the current implementation only permits one orientation vector per element. In future work, we hope to extend the model to have the capability to include multiple fiber orientations within a single finite element, which will require additional modifications to the theoretical basis. The method of diffusion spectrum imaging (DSI) is an example of where this functionality would be useful to have, since DSI is capable of describing fiber crossings.

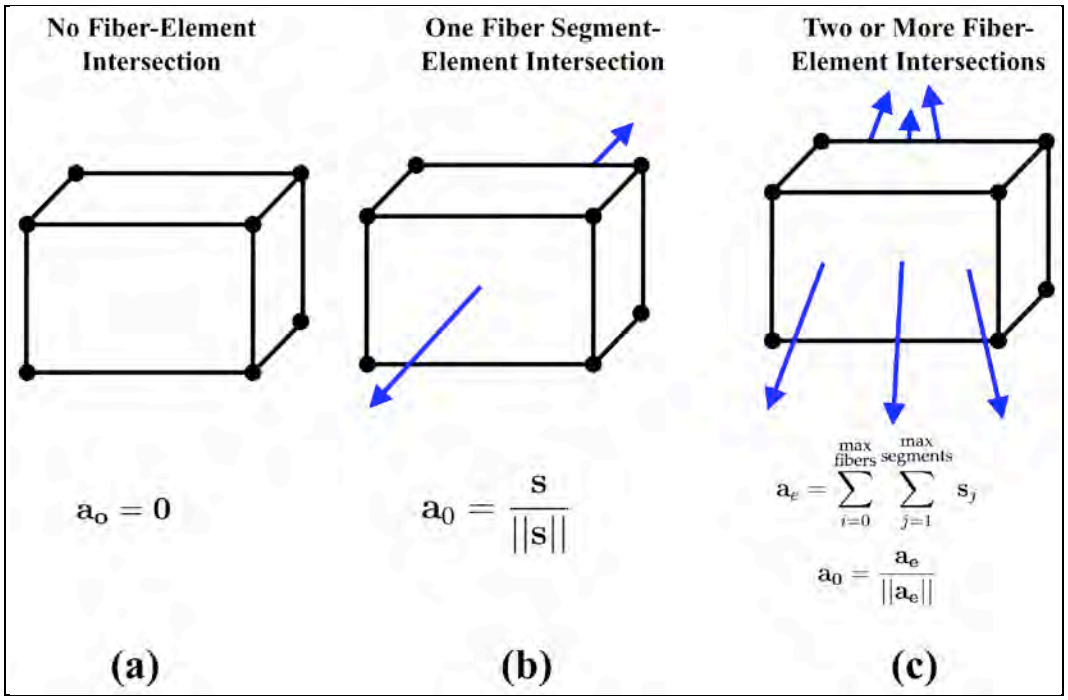

Figure 23. Depending on the fiber or mesh densities, there could be multiple fibers, or multiple fiber segments, or both existing in a single element which requires an averaging scheme.

In the case of a single fiber with multiple fiber segments within the same element, an approximation of an "average" vector direction is taken because the material model uses only one fiber direction per element. By simply adding the vectors, you obtain a resultant "average" direction, which provides an estimate of an overall fiber orientation, as schematically depicted in figure 24.

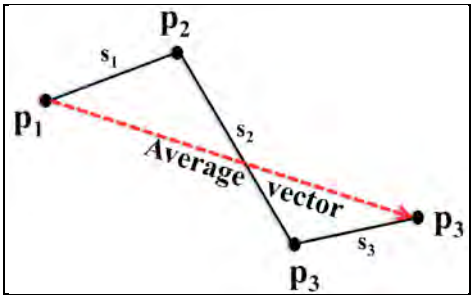

Figure 24. The sum of the vectors will give an average orientation.

For two or more fibers in a single element, the assigned orientation, $\mathbf{a}_0$, is calculated by the following:

$$\mathbf{a}_e = \sum_{i=0}^{\substack{\max \\ \text{fibers}}} \sum_{j=1}^{\substack{\max \\ \text{segments} \\ \text{in fiber i}}} \mathbf{s}_{[j][i]} \tag{60}$$

$$\mathbf{a_0} = \frac{\mathbf{a_e}}{||\mathbf{a_e}||} \tag{61}$$

where s_j are the orientation vectors of the fiber segments within the element and $\mathbf{a}_e$ represents the average of s_j—two averages are taken with each element. First, the vectors from the segments, s_j , within the same fiber line and element are averaged. Second, the average of all fibers within that element are calculated. Because the fiber average scheme depends on the element size, future efforts will explore the effects of finite element mesh density. A course finite mesh decreases computational cost, but may also smear out the complex fiber orientations. However, there are regions of the fiber tractography that change slowly over spatial distance so a course mesh may be more appropriate. The preceding procedures for determining an element orientation for the transverse isotropic model can be summarized by the global algorithm shown in figure 25.

```
for each element
    for each fiber
        for each segment in fiber
            Determine case for fiber points
            Store segment orientation vector s
        end
        Sum segment vectors for given element and fiber
    end
    Compute a_e (Sum orientation vectors for all fibers in element)
    Compute a_0
end
```

Figure 25. The global algorithm used to obtain final vector orientations for each element.

Although this method will automatically take into account the vector magnitudes, one limitation of this approach involves the loss of orientation information due to the averaging scheme for adjacent fiber segments that are close to perpendicular. For example, as shown in figure 26, if one point of the fiber segment, p_1, is entirely outside of the element, while the other point of the segment, p_2, is inside the element but relatively close to the element's surface, that fiber segment direction will receive more weight than it should. It receives the same amount of weight as it would if it were fully contained within the element. Although the accuracy of the fiber representation is limited by the mesh resolution, it is possible in the future to create a more accurate averaging of fiber directions in each element.

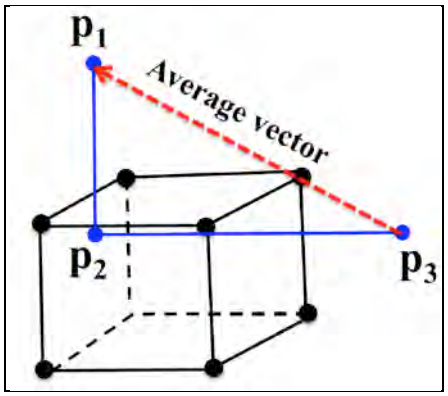

Figure 26. Averaging fibers that are not fully contained in the element can create a misrepresented average direction for the individual element.

To visualize the assigned element fiber directions, the unit vector was scaled by a characteristic length of the element (diagonal or side length) and added to the center coordinates of each element. The Visualization ToolKit (VTK) output file describes the lines connecting the center positions and endpoints of the scaled unit vectors, which can be opened up in Paraview (Kitware) and then compared against the original dataset. The visualization lines are not meant to completely coincide with the input fiber lines but rather represent the directions assigned to each element. Since the visualization lines are positioned at the center of each element, the lines will be in close proximity to the fiber lines they represent, but will not be exactly overlapping. A higher resolution mesh will produce a more accurate representation of fiber direction assignment to the elements.

5.3.5 Application to Modeling White Matter Tissue of the Human Brain

The primary objective of implementing the transverse isotropic model was to incorporate fiber directions into the finite element models for application to anisotropic biological tissue. Multiple scenarios were created to test the algorithms; however, instead of presenting the exhaustive list here, only the brain model is shown. Figure 27a shows the input fiber tractography superimposed with a finite element mesh of the human brain. Figure 27b shows the fiber orientations assigned to the elements, obtained from the fiber tractography. While this example shows qualitative agreement, it is important to note that the finite element mesh and the fiber tractography are not from the same individual at this time. There is currently a major focus to develop models from a single individual.

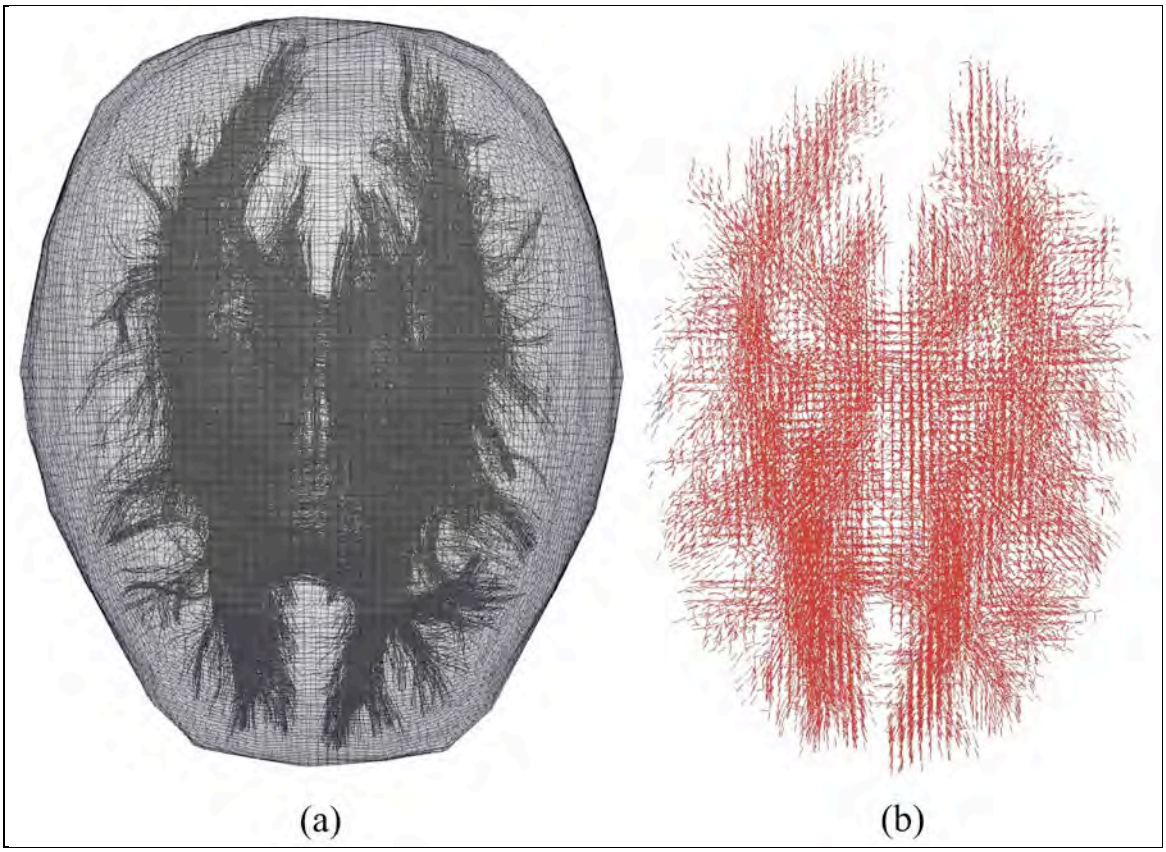

Figure 27. DTI input data versus the assigned orientation output.

5.4 Conclusions

The work presented here provides a novel way to use state-of-the-art medical imaging to inform a three-dimensional transversely isotropic model of biological tissue. After testing the numerical model's implementation, an algorithm was created in order to read fiber data and output the undeformed fiber directions into the material model. The initial results are promising since they qualitatively show adequate correlation between the original DTI data and the averaged directions that were assigned to the elements. The DWI-informed modeling can be extended to other biological tissues and different material models. Aside from using DTI for imaging the white matter of the brain, it can also measure skeletal muscle fiber directions in fixated skeletal muscles. Additionally, the model could be useful for finite element modeling of non-biological fibrous materials, such as Kevlar and various synthetic polymers.

As mentioned earlier, future work will include finite element models that correspond to the MRI data and DTI data derived from the same individual. The algorithm could be improved by constantly updating the fiber directions, which may change during deformation, although this would most likely increase the overall time required to run the simulation and may not be necessary for simulations of short events, such as blast or impact loading. Furthermore, DSI images maybe incorporated into the computational framework so that fiber crossings may also be included.

6. Conclusion

This DSI research effort in Brain Structure-Function Couplings aims to develop a multidisciplinary, multiscale understanding of the relationship between the brain's physical structure, its dynamic electrochemical functioning, and human behavior. This report provides an overview of the program to capture the general direction of this evolving program as well as four project descriptions to highlight a subset of Year 1 accomplishments in the program.

The descriptions for Project 1 and Project 2 highlight the development and assessment of a time-evolving functional measure, WPLI. The complementary results suggest that WPLI may have advantages over traditional approaches when the data set has large-scale movement artifacts, and time-evolving WPLI holds promise for understanding brain function in complex operational environments with real-world eye and body movements, providing a critical tool for the development of neurotechnologies that could monitor neural data in real time to augment Soldier-system performance.

The descriptions for Project 3 and 4 highlight accomplishments under the program's two modeling efforts. The electrochemical structure-function modeling results indicate that the three phase measures tested (ImC, dWPLI, and PLV) do capture the temporal dynamics of the communication between nodes, but even in two-node networks, the results indicate that network structure strongly influences the measure results and suggests relationships between structure and function need to be explored further. The biomechanical structural modeling effort results describe a method for incorporating empirically collected white matter tract data (DWI) into a finite element model. This work lays the critical foundation needed to increase the fidelity of the brain tissue response in simulations of tissue damage due to blast or blunt forces.

Collectively, these four projects capture the research enhancements derived through cross-Directorate collaboration. The simulated EEG data can be used to validate and better understand functional measures that are tested on empirical datasets. The imaged brain structure is incorporated into a finite element model to increase the fidelity of the simulated tissue response properties. Critically, in our first year, each of the four efforts has successfully incorporated a graph theoretic framework to ensure advancements between areas can be integrated as the research develops in the years to come.

7. References

Albert, R.; Barabasi, A. L. Statistical Mechanics of Complex Networks. *Reviews of Modern Physics* **2002**, *74*, 47–97.

Arbogast, K. B.; Margulies, S. S. A Fiber-reinforced Composite Model of the Viscoelastic Behavior of the Brainstem in Shear. *Journal of Biomechanics* **1999**, *32*, 865–870.

Bassett, D. S.; Brown, J. A.; Deshpande, V.; Carlson, J. M.; Grafton, S. T. Conserved and Variable Architecture of Human White Matter Connectivity. *NeuroImage* **2011**, *54* (2), 1262–79. doi:10.1016/j.neuroimage.2010.09.006.

Bassett, D.; Wymbs, N. F.; Porter, M. A.; Mucha, P. J.; Carlson, J. M.; Grafton, S. T. Dynamic Reconfiguration of Human Brain Networks During Learning. *PNAS* **2011**. doi:10.1073/pnas.1018985108.

Bengtsson, S. L.; Nagy, Z.; Skare, S.; Forsman, L.; Forssberg, H.; Ullén, F. Extensive Piano Practicing has Regionally Specific Effects on White Matter Development. *Nature Neuroscience*. **2005**, *8*, 1148–1150.

Berger, H. Uber das elektrenkephalogramm des menschen. *Archiv fur Psychiatrie und Nervenkrankheiten* **1929**, *87*, 527.

Börner, K.; Sanyal, S.; Vespignani, A. Network Science. I*n B. Cronin (Ed.), Annual Review of Information Science and Technology*, Vol. 41, Chapter 12, pp. 537-607. Medford, NJ: Information Today, Inc./American Society for Information Science and Technology, 2007.

Bressler, S. L. Large-scale Cortical Networks and Cognition. *Brain Research Reviews* **1995**, *20*, 288–304.

Bressler, J. L.; Menon, V. Large-scale Brain Networks in Cognition: Emerging Methods and Principles. *Trends in Cognitive Sciences* **2006**, 14, 277–290.

Bressler, S. L.; Tognoli, E. Operational Principles of Neurocognitive Networks. *International Journal of Psychophysiology* **2006**, *60*, 139–148.

Bullmore, E.; Sporns, O. Complex Brain Networks: Graph Theoretical Analysis of Structural and Functional Systems. Nature reviews. *Neuroscience* **2009**, *10* (3), 186–98. doi:10.1038/nrn2575.

Bullmore, E. T.; Bassett, D. S. Brain Graphs: Graphical Models of the Human Brain Connectome. *Annual Review of Clinical Psychology* **2011**, *7*, 2.1–2.28.

Butts, C. T. Revisiting the Foundations of Network Analysis. *Science* **2009**, *325*, 414-416.

Cascio, C. J.; Gerig, G.; Piven, J. Diffusion Tensor Imaging: Application to the Study of the Developing Brain. *J Am Acad Child Adolesc Psychiatry* **2007**, *46*, 213–223.

David, O.; Friston, K.J. A Neural Mass Model for MEG/EEG: Coupling and Neuronal Dynamics. *NeuroImage* **2003**, *20* (3), 1743–1755.

Delorme, A.; Makeig, S. EEGLAB: An Open Source Toolbox for Analysis of Single-trial EEG Dynamics Including Independent Component Analysis. *Journal of Neuroscience Methods* **2004**, *134*, 9–21, http://sccn.ucsd.edu/eeglab/index.html.

EFPL. The Blue Brain Project, 2011. http://bluebrain.epfl.ch (accessed Jan 2012).

Engel, A. K.; Fries, P.; Singer, W. Dynamic Predictions. *Nature Reviews Neuroscience* **2001**, *2*, 704–716.

Fries, P. A Mechanism for Cognitive Dynamics: Neuronal Communication Through Neuronal Coherence. *Trends in Cognitive Sciences* **2005**, *9* (10), 474–80.

Friston, K. J. Functional and Effective Connectivity in Neuroimaging: A Synthesis. *Human Brain Mapping* **1994**, *2*, 56–78.

Gevins, A.; Leong, H.; Du, R.; Smith, M. E.; Le, J.; DuRousseau, D.; Zhang, J.; Libove, J. Towards Measurement of Brain Function in Operational Environments. *Biological Psychology* **1995**, *40*, 169-186.

Gibson, J. J. *The theory of affordances. Perceiving, Acting, and Knowing: Toward an Ecological Psychology*; Lawrence Erlbaum: Hillsdale, NJ, 1977, pp. 67–82.

Gibson, J. J. *The Ecological Approach to Visual Perception*; Houghton Mifflin: Boston, MA, 1979.

Gray, C. M.; König, P.; Engel, A. K.; Singer, W. Oscillatory Responses in Cat Visual Cortex Exhibit Inter-columnar Synchronization which Reflects Global Stimulus Properties. *Nature* **1989**, *338* (6213), 334-337.

Hagmann, P.; Jonasson, L.; Maeder, P.; Thiran, J.; Wedeen, V. J.; Meuli, R. *Understanding Diffusion MR Imaging Techniques: From Scalar Diffusion-weighted Imaging to Diffusion Tensor Imaging and Beyond Radiographics* 26:S205-S223; doi:10.1148/rg.26si065510, 2006.

Holzapfel, G. A. *Nonlinear Solid Mechanics*; John Wiley and Sons, LTD, 2000.

Honey, C. J.; Sporns, O.; Cammoun, L.; Gigandet, X.; Thiran, J. P.; Meuli, R.; Hagmann, P. Predicting Human Resting-state Functional Connectivity from Structural Connectivity. *Proceedings of the National Academy of Sciences of the United States of America*, 106(6), 2035-40. doi:10.1073/pnas.0811168106, 2009.

Izzetoglu, M.; Bunce, S. C.; Izzetoglu, K.; Onaral, B.; Pourrezaei, K. Functional Brain Imaging Using Near-infrared Technology. *IEEE Eng Med Biol Mag* 2007, *26* (4), 38–46.

Jung, T. P.; Makeig, S.; Humphries, C.; Lee, T. K.; McKeown, M. J.; Iragui, V.; Sejnowski, T. J. Removing Electroencephalographic Artifacts by Blind Source Separation. *Psychophysiology* **2000**, *37*, 163–178.

Kerick, S. E.; Hatfield, B. D.; Allender, L. E. Event-Related Cortical Dynamics of Soldiers During Shooting as a Function of Varied Task Demand, *Aviation, Space, and Environmental Medicine* **2007**, *78* (5), B153–B164.

Kingstone, A.; Smilek, D.; Ristic, J.; Friesen, C. K.; Eastwood, J. D. Attention, Researchers! It's Time to Take a Look at the Real-world. *Current Directions in Psychological Science* **2003**, *12*, 176-180.

Kingstone, A.; Smilek, D.; Eastwood, J. D. Cognitive Ethology: A New Approach for Studying Human Cognition. *British Journal of Psychology* **2008**, *99*, 317–340.

Kraft, R.; Dagro, A. *Design and Implementation of a Numerical Technique to Inform Anisotropic Hyperelastic Finite Element Models using Diffusion Weighted Imaging*; ARL-TR-5796; U.S. Army Research Laboratory: Aberdeen Proving Ground, MD, in press.

Lachaux, J. P.; Rodriguez, E.; Martinerie, J.; Varela, F. J. Measuring Phase Synchrony in Brain Signals. *Human Brain Mapping* **1999**, *8* (4), 194–208.

Le van Quyen, M. Disentangling the Dynamic Core: A Research Program for a Neurodynamics at the Large-scale. *Biological Research* **2003**, *36*, 67-88.

Lin, C. T.; Ko, L. W.; Chang, M. H.; Duann, J. R.; Chen, J. Y.; Su, T. P.; Jung, T. P. Review of Wireless and Wearable Electroencephalogram Systems and Brain-computer Interfaces - A Mini-review. *Gerontology* **2010**, *56*, 112–119.

Madden, D. J.; Bennett, I. J.; Song, A. W. Cerebral White Matter Integrity and Cognitive Aging: Contributions from Diffusion Tensor Imaging, *Neuropsychol Rev* **2009**, *19*, 415-435

Makeig, S.; Bell, A. J.; Jung, T. P.; Sejnowski, T. J. Independent Component Analysis of Electroencephalographic Data. *Advances in Neural Information Processing Systems* **1996**, *8*, 145–151.

Makeig, S.; Gramann, K.; Jung, T. P.; Sejnowski, T. J.; Poizner, H. Linking Brain, Mind and Behavior. *International Journal of Psychophysiology* **2009**, *73*, 95–100.

Ning, X.; Zhu, Q.; Lanir, Y.; Margulies, S. S. A Transversely Isotropic Viscoelastic Constitutive Equation for Brainstem Undergoing Finite Deformation. *Journal of Biomechanical Engineering* **2006**, *128*, 925–930.

Nolte, G.; Bai, O.; Wheaton, L.; Mari, Z.; Vorbach, S.; Hallett, M. Identifying True Brain Interaction from EEG Data Using the Imaginary Part of Coherency. *Clinical Neurophysiology* **2004**, *115* (10), 2292–307.

Nieuwenhuys, R.; Voogd, J.; van Huijzen, C. *The Human Central Nervous System,* 4th edition; Springer-Verlag Press: Berlin, Germany, 2008.

Nunez, P. L.; Srinivasan, R. *Electric Fields of the Brain: The Neurophysics of EEG*. Oxford University Press: New York, NY, 2006.

Oie, K.; McDowell, K. Neurocognitive Engineering for Systems Development. *Synesis* **2011**, *2*, T17–25.

Onton, J.; Westerfield, M.; Townsend, J.; Makeig, S. Imaging Human EEG Dynamics Using Independent Component Analysis. *Neuroscience and Biobehavioral Reviews* **2006**, *30*, 808–822.

Parasuraman, R. Neuroergonomics: Research and Practice. *Theoretical Issues in Ergonomics Science* **2003**, *4*, 5–20.

Parasuraman, R.; Rizzo, M. *Neuroergonomics: The brain at work*; Oxford University Press: New York, NY, 2007.

Rubinov, M.; Sporns, O. Complex Network Measures of Brain Connectivity: Uses and Interpretations. *Neuroimage* **2010**, *52*, 1059–1069.

Scholz, J.; Klein, M. C.; Behrens, T.E.J.; Johansen-Berg, H. Training Induces Changes in White-matter Architecture. *Nature Neuroscience* **2009**, *12*, 1370–1371.

Sporns, O.; Tononi, G.; Edelman, G. M. Connectivity and Complexity: The Relationship Between Neuroanatomy and Brain Dynamics. *Neural Networks* **2000**, *13*, 909–922.

Stam C. J.; Jones, B. F.; Nolte, G.; Breakspear, M.; Scheltens, P. Small-Word Networks and Functional Conectivity in Alzheimer's Disease, *Cerebral Cortex* **2007**, *17*, 92–99.

Stam, C. J.; Nolte, G.; Daffertschofer, A. Phase Lag Index: Assessment of Functional Connectivity from Multi Channel EEG and MEG with Diminished Bias from Common Sources, *Hum. Brain Mapp.* **2007**, *28* (11), 1178–1193.

Taber, K. H.; Warden, D. L.; Hurley, R. A. Blast-related Traumatic Brain Injury: What is Known? *J Neuropsychiatry Clinical Neuroscience* **2008**, *18*, 141–145.

U.S. Department of the Army. Use of Volunteers as Subjects of Research. AR 70-25. Government Printing Office: Washington, DC, 1990.

U.S. Department of Defense. Code of Federal Regulations: Protection of Human Subjects. 32 CFR 219, Office of the Secretary of Defense. Government Printing Office: Washington, DC, 1999.

Verstynen, T.; Jarbo, K.; Puthak, S.; Schneider, W. In Vivo Mapping of Microstructural Somatotopies in the Human Corticospinal Pathways. *J Neurophysiol* **2011**, *105*, 336–346, 2011

Vinck, M.; Oostenveld, R.; van Wingerden, M.; Battalglia, F.; Pennartz C.M.A. An Improved Index of Phase-Synchronization for Electrophysiological Data in the Presence of Volume-Conduction, Noise, and Sample-Size Bias. *NeuroImage* **2011**, *55* (4), 1548-156

Weiss, J. A.; Maker, B. N.; Govindjee, S. Finite Element Implementation of Incompressible, Transversely Isotropic Hyperelasticity. *Computer Methods in Applied Mechanics and Engineering* **1996**, *135*, 107–128.

Wright, R.; Ramesh, K. An Axonal Strain Injury Criterion for Traumatic Brain Injury. *Biomechanics and Modeling in Mechanobiology* **2011**, *11* (1-2), 1-16; 10.1007/s10237-011-0307-1.

Xu, J.; Li, Y.; Lin, H.; Sinha, R.; Potenza, M. N. Body Mass Index Correlates Negatively with White Matter Integrity in the Fornix and Corpus Callosum: A Diffusion Tensor Imaging Study. *Human Brain Mapping* **2011**. doi: 10.1002/hbm.21491.

Lists of Symbols, Abbreviations, and Acronyms

ARL	U.S. Army Research Laboratory
BSFC	brain structure-function couplings
CISD	Computational and Information Sciences Directorate
CTA	Collaborative Technology Alliances
DRC	Dynamics Research Corporation
DSI	Director's Strategic Initiative
DTI	diffusion tensor magnetic resonance medical imaging
DWI	diffusion-weighted imaging
dWPLI	debiased weighted phase lag index
EEG	electroencephalography
FA	fractional anisotropy
FIR	finite impulse response
fMRI	functional magnetic resonance imaging
fNIR	functional near-infrared spectroscopy
HRED	Human Research and Engineering Directorate
Hz	hertz
ICA	independent component analysis
ICB	Institute for Collaborative Biotechnologies
ICs	independent components
ImC	imaginary component of coherence
LFP	local field potential
MEG	magnetoencephalography
MRI	magnetic resonance imaging
MRMC	Medical Research and Materiel Command

MURI	Multidisciplinary University Research Initiative
NFFT	nonequispaced fast Fourier transform
NMM	neural mass model
OSTP	Office of Science and Technology Policy
PLI	phase lag index
PLV	phase lag value
PSD	power spectral density
UCSB	University of California at Santa Barbara
USMA	United States Military Academy
VTK	visualization toolkit
WMRD	Weapons and Materials Research Directorate
WPLI	weighted phase lag index

NO. OF COPIES	ORGANIZATION
1	ADMNSTR
ELEC	DEFNS TECHL INFO CTR ATTN DTIC OCP 8725 JOHN J KINGMAN RD STE 0944 FT BELVOIR VA 22060-6218
3	US ARMY RSRCH LAB ATTN IMNE ALC HRR MAIL & RECORDS MGMT ATTN RDRL CIO LL TECHL LIB ATTN RDRL CIO MT TECHL PUB ADELPHI MD 20783-1197
8	US ARMY RSRCH LAB ATTN RDRL HRS C JEAN VETTEL STEPHEN GORDON SCOTT KERICK SANDHYA RAWAL KALEB MCDOWELL ATTN RDRL WMP B AMY DAGRO REUBEN KRAFT ATTN RDRL-CIH-C MANNY VINDIOLA APD MD 21005
TOTAL:	12 (11 HCS, 1 ELEC)